Research Square

Preprints are preliminary reports that have not undergone peer review.
They should not be considered conclusive, used to inform clinical practice,
or referenced by the media as validated information.

Infodynamic insights applied to effervescent sprays

Miguel R.O. Panão

miguel.panao@dem.uc.pt

University of Coimbra

Ondrej Cejpek

Brno University of Technology

Milan Maly

Brno University of Technology

Jan Jedelsky

Brno University of Technology

Research Article

Keywords: Effervescent atomizer, Infodynamics, Droplet Size Distribution, Info-hollow cone spray

Posted Date: November 17th, 2026

DOI: https://doi.org/10.21203/rs.3.rs-11527448/v1

License: This work is licensed under a Creative Commons Attribution 4.0 International License.
Read Full License

Additional Declarations: No competing interests reported.

Infodynamic insights applied to effervescent sprays

Miguel R.O. Panão[1*], Ondrej Cejpek[2], Milan Malý[2], Jan Jedelský[2]

[1*]Department of Mechanical Engineering, ADAI-LAETA, University of Coimbra, Polo II, Rua Luis Reis Santos, 3030-788, Coimbra, Portugal.
[2]Energy Institute, Brno University of Technology, Technická 2, 616-69, Brno, Czech Republic.

*Corresponding author(s). E-mail(s): miguel.panao@dem.uc.pt;
Contributing authors: Ondrej.Cejpek@vutbr.cz; milan.maly@vutbr.cz; jedelsky@fme.vutbr.cz;

Abstract

The characterization of effervescent atomizers, useful for atomizing viscous liquids, and that of sprays in general, often reduce droplet size distributions to mean diameters that cannot express the diversity and indeterminacy inherent to atomization. This study introduces an infodynamic characterization layer built on known information theory parameters, such as informature $\boldsymbol{H_I}$, differential informature $\boldsymbol{H_\Delta}$, and newly developed, as the Representation Index $\boldsymbol{R_{(j)}}$. Informature quantifies the amount of information carried by number-, area-, and volume-weighted droplet size distributions, but depends on the measurement alphabet (i.e., statistical classes). The differential informature proves essentially alphabet-independent, and is an intensive descriptor of the spray informational structure. The Representation Index quantifies the invariance between regular and variable size classes to locate the dominant information carried by droplets, among that of number, interfacial area, and liquid volume. $\boldsymbol{R_{(j)}}$ depends on the resolution scale of the measurement technique, and its spread across these carriers reveals whether they reside at separated scales. Applied to Phase Doppler Interferometry measurements of an effervescent atomizer at several gas-to-liquid ratios (GLR), the framework uncovers an "info-hollow-cone" informational structure: differential informature peaks at the spray/ambient interface, locating the spray boundary from the droplet size distribution alone, while $\boldsymbol{R_{(j)}}$ profiles resolve three radial regions and a progressive depletion of volume carriers from the spray axis as GLR increases, which follows the decrease of their geometric mean diameter below the reference scale of the measurement.

Keywords: Effervescent atomizer, Infodynamics, Droplet Size Distribution, Info-hollow cone spray

1 Introduction

Effervescent atomizers, a type of twin-fluid atomizer with internal mixing, are viable options for industrial processes that require the atomization of viscous fluids, well-atomized sprays with a large interfacial area, or fine droplets with controllable momentum. Such requirements arise in food processing, combustion systems, spray scrubbing, and spray coating, among other fields. Compared to single-fluid atomizers, effervescent atomizers can vary the amount of atomizing gas, particularly the gas-to-liquid ratio (GLR), to control the atomization process. Effervescent atomizers were first introduced by Lefebvre (1988) and have since been continuously developed by several research groups (Roesler and Lefebvre 1989; Sovani et al. 2001; Jedelský et al. 2009, 2014). This atomization strategy is a well-established method for spray systems. However, the indeterminacy of drop formation is not yet fully understood, nor is it accounted for in their design. By "indeterminacy", we mean the natural diversity a physical system generates, such as that found in liquid atomization and sprays. It is not measurement scatter, nor the dispersion that a probability density function conventionally expresses. Under fixed operating conditions, and with complete knowledge of the injector geometry, atomization does not produce a single droplet size but a diversity of sizes, and this diversity has a physical origin: ligament breakup amplifies corrugations too small to be specified, implying that nominally identical events yield different droplet populations (Villermaux et al. 2004), and in effervescent atomizers the discharge alternates chaotically between gas- and liquid-dominant jets in the slug regime (Malý et al. 2025).

In the approach engineering does to uncertainty, such diversity is random rather than epistemic (Der Kiureghian and Ditlevsen 2009), which means more data or a better model will not remove it, because it belongs to the system and not to our knowledge of it. Spray science has long acknowledged this implicitly, considering how the Maximum Entropy Formalism closes the atomization problem because droplet formation cannot be deduced from hydrodynamics alone (Li and Tankin 1992; Dumouchel 2009). However, that formalism uses information theory to predict the most probable distribution under a set of constraints, prescriptively, whereas Panão (2025b) showed that formulating the physical problem itself exposes the mechanism(s) at the origin of the resulting distribution. Therefore, a measured droplet size distribution carries physical content that its moments do not express, which is the premise of the infodynamic approach developed here.

Droplet size diversity begins inside the atomizer. The liquid atomization process in effervescent sprays is governed by internal two-phase flow. Its structure is sensitive to the inlet pressure (p_{in}), GLR, and atomizer geometry (Hammad et al. 2021). It may appear as a flow of bubbles (low GLR), slugs (intermediate GLR), or an annular flow regime (high GLR) (Sun et al. 2019). In all cases, however, liquid breakup into small droplets is caused by the rapid expansion of the gaseous phase, which tears the liquid into ligaments and subsequently fragments them into droplets, as described by Zaremba et al. (2018). When slug flow is present, the discharge alternates between gas-dominant and liquid-dominant jets (Malý et al. 2025). With a further increase in the GLR, an annular internal flow is established, which discharges a thin annular liquid film with a high-speed gas core (Zaremba et al. 2018). Therefore, the internal flow

alters the atomization process, which leads to diverse droplet sizes, velocities, and corresponding distributions, usually measured in the fully developed spray, considerably downstream of the atomizer.

A significant number of events occur between the discharge and the measurement position. Rapid momentum exchange between the liquid, atomization gas, and surrounding environment occurs after the discharge. In the vicinity of the atomizer, a large relative velocity between the gas and liquid creates strong shear-disruptive forces. As the atomizing gas decelerates downstream, the strong initial gas–liquid shear transfers momentum to the dispersed phase, accelerating the droplets, particularly those with low Stokes numbers, and entraining them toward the spray core (Cejpek et al. 2026). As the liquid and atomization gas velocities become equal at some point downstream from the atomizer, the interaction with the surrounding environment dominates, causing agglomeration or clustering of droplets at the spray boundary induced by outer gas vortices (Heinlein and Fritsching 2006). Further downstream from the atomizer, the droplets reach their terminal falling velocity (Beard 1976). Understanding the development of the liquid velocity matters because it governs the stand-off distance required to achieve the desired deposition regime in spray coating, and the contact time that maximizes performance in spray scrubbing.

Primary liquid atomization and liquid–gas interactions are crucial for droplet formation and spatial distribution, and they also determine how the energy supplied to the atomizer is shared between the creation of new liquid surface and the motion of the droplets. This sharing is unbalanced: as shown by Jedelský and Jicha (2013), only a few percent of the input energy is converted into droplet surface energy, whereas most of it is converted into droplet kinetic energy. Since both energies are evaluated from the droplet sizes and velocities measured in the spray, assessing the atomization efficiency, and improving it, depends on the accuracy of these data. That accuracy is limited by the choice of measurement technique, as each technique is suited to droplets generated by different mechanisms. Therefore, a better understanding of atomization physics and injector design requires an accurate characterization of spray dynamics, which can be achieved with the laser and imaging techniques commonly used to characterize droplets and their spatial distributions (Zaremba et al. 2018; Mlkvik et al. 2020; Cejpek et al. 2023a).

Each technique observes a different part of the spray. Phase Doppler Interferometry (PDI) can characterize small droplets inside dense sprays, whereas high-resolution high-speed visualization can better capture large nonspherical liquid structures (Sijs et al. 2021; Cejpek et al. 2023b). We focused on Phase Doppler Interferometry (PDI) because of its temporal resolution, and because it measures the size and velocity of each droplet simultaneously. Moreover, the selection of a representative measurement position is crucial. There are cases where a single-point measurement, preferably in the spray center, is sufficient (Hammad et al. 2021). Data from a single point characterize the spray locally, even when conclusions about the spray as a whole are drawn from them. The application of line-of-sight methods integrates droplets over the entire measurement volume along the beam path, effectively averaging the spatial variations in droplet size but losing information about the droplet-size distribution across the

spray (García et al. 2017; Wittner et al. 2019). In most industrial processes, droplet size is the main parameter used to describe a spray.

Nonetheless, a spray is never a single size. In the case of liquid atomization, although measurement techniques can acquire data on the multiple sizes of droplets, a single parameter often replaces the measured droplet size distribution (DSDn). The most common analysis examines how operating parameters affect mean diameter values. Each mean diameter has a specific meaning in terms of spray characterization. For example, the arithmetic mean diameter (D_{10}) is equivalent to the size of all counted droplets if they were equal. The Sauter Mean Diameter (D_{32}), often used in combustion applications, is the mean diameter of an area-weighted DSDn; it is physically related to atomization efficiency (Panão 2022) and is taken to represent the spray area. The volume-weighted mean diameter (D_{43}) represents the DSDn volume and mass, which is relevant for spray cooling applications. If j represents the weight with which we build a DSDn ($j = 0$ ≡number-, $j = 2$ ≡area-, $j = 3$ ≡volume-weighted), the relative frequencies are generally expressed as

$$\omega_{j,i} = \frac{n_i d_i^j}{\sum_{i=1}^{k} n_i d_i^j} \tag{1}$$

where n_i is the number of droplets inside class i centered at d_i, k is the number of classes dividing the size range spectrum, and $\sum_i \omega_{j,i} = 1$. An l-moment of the distribution is given by

$$m_{j,l} = \sum_{i=1}^{k} \omega_{j,i} d_i^l \tag{2}$$

and the mean diameter of a j-weighted DSDn is given by

$$D_{\alpha j} = \frac{m_{j,\alpha-j}}{m_{j,0}} \tag{3}$$

For example, the Sauter Mean Diameter corresponds to

$$D_{32} = \frac{m_{2,1}}{m_{2,0}} = \frac{\sum_{i=1}^{k} \omega_{2,i} d_i^1}{\underbrace{\sum_{i=1}^{k} \omega_{2,i} d_i^0}_{=1}} = \sum_{i=1}^{k} \omega_{2,i} d_i \tag{4}$$

implying that it is the mean of an area-weighted DSDn. Mean diameters are useful for parametric analyses of how operating conditions affect liquid atomization in injector design. However, they convey no information about the diversity of drop sizes. Moreover, each weighted distribution of the same data is related to different types of information. The number-weighted DSDn carries information on the spray density, the area-weighted DSDn on the interfacial area (relevant in heat transfer applications), and the volume-weighted DSDn on the spray mass.

Drop size diversity itself has not been ignored. To obtain a glimpse of the Drop Size Diversity (DSDy), the standard deviation, $(m_{j,2} - m_{j,1}^2)^{1/2}$, obtained from the second moment $m_{j,2}$, is a possibility, but is blind to multimodal DSDn shapes. The most common parameter is probably the Relative Span Factor ($RSF = (D_{j,90} - D_{j,10})/D_{j,50}$) based on a cumulative droplet size distribution ($F_{j,i} = \sum_{s=1}^{i} \omega_{j,s}$) and three representative diameters ($D_{j,10}, D_{j,50}, D_{j,90}$, the size representing 10%, 50%, and 90% of the spray droplets organized in the j-weighted DSDn), but Panão et al. (2020) showed the limitations of the RSF. The q shape factor, interpreted as a fractal dimension when the DSDn is fitted by a Weibull distribution, is also a common measure of DSDy, as is the Geometric Standard Deviation (GSD) obtained from a log-normal fit. Both, however, assume without adequate verification that a specific probability density function (PDF) describes reality. García et al. (2017) proposed the volume-weighted Standard Deviation SD_v to assess DSDy, without assuming a certain PDF, but, like the previous proposals, it disregards the actual shape and scale of the measured DSDn [see also Roesler and Lefebvre (1989); Hammad et al. (2021); Schröder et al. (2011); Rosell-Llompart and Gañán-Calvo (2008)]. Like the mean quantities, these approaches do not fully capture the amount of information contained in droplet size distributions of different shapes, including multimodal ones. This study argues that capturing the diversity underlying spray indeterminacy, hidden by the mean quantities and moments of the droplet size distribution, implies adding a new layer to spray characterization based on the amount of information available, as explained in the next section.

2 A New Spray Language and Characterization Layer

Spray dynamics are typically characterized by measuring drop size, velocity, and flux. The analysis usually focuses on mean quantities, which are useful for providing data to validate numerical models. However, although the mean quantities are sensitive to the indeterminacy of the spray dynamics, they do not accurately express it. In this study, we argue for adding an essential layer to spray characterization, one that captures this indeterminacy. Panão (2025b); Ferrão et al. (2025) have previously demonstrated that infodynamics provides quantified measures of a spray's indeterminacy, using parameters such as *informature* that quantify the amount of information regardless of its context. Therefore, in this section, we show why infodynamic parameters add a new and independent layer to spray characterization, one that brings spray indeterminacy into the validation of numerical models and offers deeper insight into spray diversity. The first step is to revise the language of spray characterization so as to highlight the link between its informational and physical nature.

A spray made of N discrete particles, each essentially described by size and velocity, $x_i \equiv (d_i, \mathbf{u}_i)$, is analogous to a gas in that it is an ensemble of many entities whose individual identities rarely matter, only their statistical regularities. Therefore, the spray *microstate* is a complete list of droplet-level states in our sample, $\Omega \equiv \{(d_1, \mathbf{u}_1), (d_2, \mathbf{u}_2), ..., (d_N, \mathbf{u}_N)\}$. To characterize the spray *macrostate*, we first define a *measurement alphabet*: the set of classes, or bins, used to organize the spray data into histograms.

Two methods are available for building the "letters" of the measurement alphabet. The first uses regular (uniform) classes of equal width, and the second uses variable (non-uniform) classes. Both are examined in Sec. 3. Given the measurement alphabet, the *macrostate* of the spray is defined by the distribution of droplet characteristics in terms of relative frequency, as shown in Eq. (1), or in terms of probability density if $\omega_{j,k}$ is divided by the class size (Δd_k) as $p_{j,k} = \omega_{j,k}/\Delta d_k$. The probability density is crucial for comparing spray macrostates because two researchers measuring the same spray microstates will report visually different macrostates if their measurement alphabets differ. This clarification is essential for understanding spray indeterminacy from an infodynamic perspective.

Shannon (1948) introduced a way to measure the amount of information required to describe a system. Naming that formulation *entropy*, on account of its formal similarity to the expression developed by J.W. Gibbs, has proved misleading. Panão (2025a) argued for restricting the term entropy to thermodynamics and proposed two others belonging to the distinct discipline of Engineering Infodynamics: *informature* and *infotropy*. This study focuses on *informature* as a new spray characteristic and demonstrates that it is an independent parameter, even though it is based on the morphological (size) or kinematic (velocity) components of each droplet-event in the spray.

Informature is an extensive informational property of a stochastic physical system, regardless of its context[1], given in the natural logarithm base by

$$H_{I,j} = -\sum_{i=1}^{k} \omega_{j,i} \ln(\omega_{j,i}) \tag{5}$$

measured in "nats"[2]. This implies that it depends on the measurement alphabet and its k "letters." Its conversion into an intensive property of the system is derived in Panão (2025b) and yields the *differential* informature, which adds to the informature a grid term, G_j, the mean logarithm of the class widths weighted by the relative frequencies,

$$H_{\Delta,j} = -\sum_{i=1}^{k} \omega_{j,i} \ln(p_{j,i}) = H_{I,j} + \underbrace{\sum_{i=1}^{k} \omega_{j,i} \ln(\Delta d_i)}_{G_j} \tag{6}$$

Since Δd_i carries units, G_j, and with it $H_{\Delta,j}$, depends on the unit of d, which is μm throughout this work. What is the value of using informature or differential informature as a new spray characteristic? As noted by Panão (2025b), informature, as a quantifiable value containing complete information on droplet size distribution, can improve our understanding of the complex interplay between atomization and liquid–gas interactions by measuring their natural diversity. Furthermore, we suggest that this information can be used for a more precise validation of numerical simulations or analytical solutions (Park et al. 2024).

[1] Context-independent means that one can apply this formulation to anything described statistically by a histogram of relative frequencies.

[2] Shannon's formulation used the base-2 logarithm, measuring the amount of information in "bits" for *bi*nary uni*ts*. The term "nats" stands for *na*tural uni*ts*.

Once the informational macrostate of the spray has been measured from a data sample (e.g., droplet size), how many classes does it actually take to carry that information? A measurement alphabet declares k classes, but a spray rarely activates all of them, because its DSDn is not uniform ($\omega_{j,i} \neq$ const.). The informature attains its maximum when every class has the same relative frequency, in which case $H_{I,j} = \ln(k)$. Inverting this relation for a measured, non-uniform distribution gives

$$k_{eff,j} = \exp\left(H_{I,j}\right) \tag{7}$$

which we designate the number of *effective classes* of the j-weighted DSDn. Since the informature measures the average degree of surprise of the distribution, $\exp(H_{I,j})$ is the number of equally probable classes that would produce the same average degree of surprise. This number is not, in general, an integer, and its fractional part is retained because it carries the information of interest: $k_{eff,j} = 1$ only when all the information resides in a single class, as in a deterministic sample, whereas $k_{eff,j} = 1.75$ already indicates a partially activated second class, and rounding down would make the two indistinguishable. It thus counts the classes that genuinely carry information, irrespective of how many were declared in the measurement alphabet, and how many classes are effective depends on the j-weight of the DSDn. Each data sample carries information on these three perspectives, but at which scales does each of them reside? The answer is in the implications of our measurement alphabet choice to characterize the spray.

3 Implications of Measurement Alphabet on Spray Characterization

The measurement alphabet defines the number of classes in the model. One of the proposed strategies for building variable-size classes is based on the interlaced Fibonacci series. Following Chang et al. (1991) and Zhang et al. (1992), the number of interlaced Fibonacci series is J, and the number of classes is obtained by rounding down to the nearest integer (*e.g.,* using the MATLAB function `floor`) as

$$k = \left\lfloor \frac{\ln(SR)}{\ln(R_e)} \right\rfloor \tag{8}$$

with $SR = D_{max}/D_{min}$ as the size range, where D_{max} and D_{min} are the maximum and minimum measurable droplet sizes, $R_e = \varphi^{1/(3 \cdot J)}$ is the average ratio between adjacent class limits, and $\varphi = (1 + \sqrt{5})/2$ is the golden ratio. The measurement alphabet is therefore defined over the measurement domain of the technique rather than over the range of sizes observed in a particular spray: the largest measurable droplets are rarely recorded, but they belong to what the technique can measure. For the PDI configuration used here, the lower end of this domain is set by the approach of droplet sizes to the laser wavelength, which fixes $D_{min} = 1$ μm as the lower edge of the geometric progression (Sec. 5), and its upper end is the maximum diameter allowed by the optical configuration, $D_{max} \approx 403$ μm. Classes within this domain

that receive no droplets are retained, since symbols of zero probability belong to the alphabet without contributing to the informature. The alphabet thus expresses the maximum amount of information that the technique can deliver on droplet size, $\ln k$, independently of the spray. The simulated distributions of this section are read with the same alphabet, as if they had been measured with this instrument, so that every example of this work, simulated or measured, refers to the same measurement domain.

To understand the implications of the measurement alphabet on spray characterization, we simulated a Log-normal DSDn with a median of $D_{50} = 50$ μm and standard deviation of $s = 1/\sqrt{6}$. A sample of $N = 10^5$ droplets, with sizes between 5.3 and 318.7 μm, was generated at random in MATLAB and classified with the measurement alphabet of the PDI instrument. Considering $J = 3$ interlaced Fibonacci series, the number of "letters" (classes) is $k = 112$. Fig. 1 exemplifies the results obtained for the number ($j = 0$)-weighted DSDn.

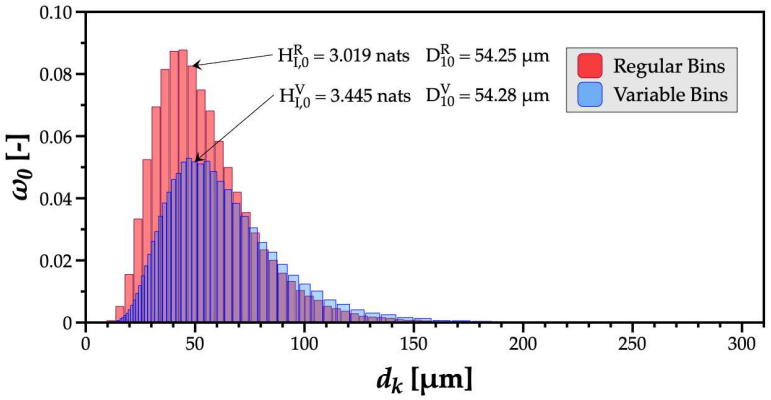


Fig. 1 Example of a number($j = 0$)-weighted Droplet Size Distribution, including information of the mean diameter and the informature values considering regular ($H^R_{I,0}$), and variable ($H^V_{I,0}$) bin sizes. It shows how similar mean diameters can correspond to different amounts of information.

The mean diameters obtained with Eq. (3) are practically identical, $D_{10} \simeq 54$ μm, yet the same data organized with different measurement alphabets produce two distinct DSDn in shape and scale. This difference is captured by the informature, which is larger for the DSDn built with variable bins. Both histograms are normalized, $\sum_i \omega_{0,i} = 1$, so the informature does not measure the area under them, which is the same, but how this unit probability is spread over the k classes: from zero, when a single class contains all droplets, to $\ln k$, when all classes are equally populated. Regular classes have a constant width, whereas variable classes widen with the diameter, so they are narrower than the regular ones at small sizes and wider at large ones. Most droplets of this distribution are small, so the variable classes resolve them more finely, the same droplets spread over more classes, and the informature increases. The diameter at which the two widths coincide is derived below, in Eq. (11). However, considering the three types of weights in DSDn ($j = 0, 2, 3$) and the different measurement alphabets (regular and variable bins), Fig. 2(a) shows that the variable bins

maintain the shape and scale of the distribution while shifting each D_{mj} determined using Eq. (3) to larger values. Regular bins, in Fig. 2(b), lead to different droplet size distributions with different amounts of information, although the mean diameters are practically the same as those obtained with the variable bin measurement alphabet. The same droplets, classified with the two measurement alphabets, therefore return mean diameters that agree within 0.3%, yet different informatures. This difference is not a discretization error. Since variable classes are narrower than regular ones at small sizes and wider at large ones, the informature is larger with variable classes when the weighted distribution is dominated by small droplets, and larger with regular classes when it is dominated by large ones: $H^V_{I,0} - H^R_{I,0} = +0.29$ nats for the number-weighted distribution in Fig. 1, whereas $H^V_{I,3} - H^R_{I,3} = -0.07$ nats for the volume-weighted distribution in Fig. 2. The disagreement between alphabets thus tells whether each kind of information is carried by small or large droplets, which no mean diameter can do, and it is the basis of the Representation Index developed below.

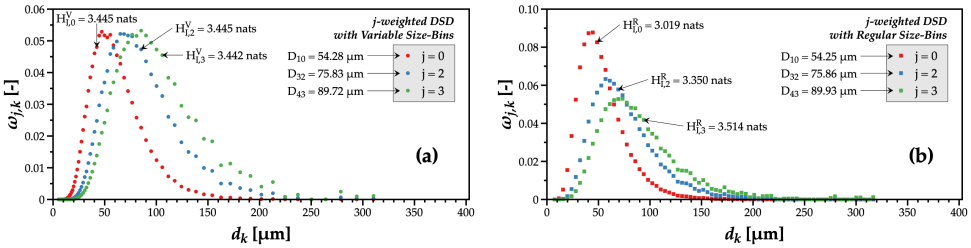


Fig. 2 Example of a number($j = 0$)-, area($j = 2$)-, and volume($j = 3$)-weighted Droplet Size Distributions, using all variable (a) and regular (b) bins. The plots include information on both mean diameter and informature values ($H^V_{I,j}$ and $H^R_{I,j}$).

If we express the droplet size distributions in terms of probability density and consider the intensive form for the amount of information, the differential informature, Fig. 3(a) shows that the number-, area-, and volume-weighted DSDn no longer depend on the measurement alphabet, and the differential informature, which includes the grid term G_j (Panão 2025b), is also independent of the measurement alphabet. The insight is that analyzing the differential informature in sprays is a more appropriate parameter to include in the new spray characterization knowledge layer.

In the next simulated experiment, we considered the mixing of two Log-normal distributions, $w = 92\%$ of one with $D_{50,1} = 30$ μm and $s_1 = 0.35$, and the remaining 8% of another with $D_{50,2} = 180$ μm and $s_2 = 0.25$. Of the $N = 2 \times 10^5$ droplets generated, the 11 larger than D_{max} (0.006%) were discarded, since the instrument would not validate them. Fig. 3(b) shows that the differential informature values are still similar regardless of the measurement alphabet (regular or variable bins).

Fig. 4 further shows how the mean size of each j-weighted distribution is similar and independent of the measurement alphabet, but the scale and shapes of these distributions are clearly different and fully captured by the informature value in its extensive form given by Eq. (5).

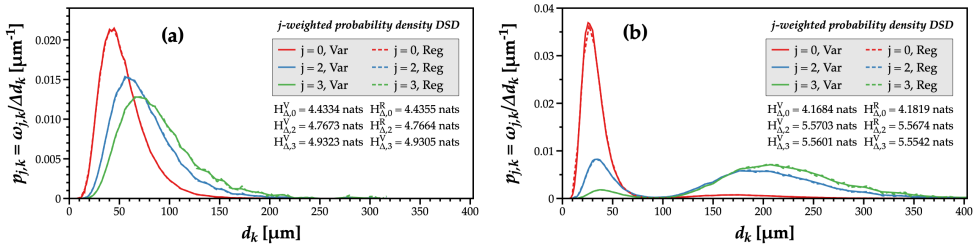


Fig. 3 Number($j = 0$)-, area($j = 2$), and volume($j = 3$)-weighted probability density droplet size distributions, considering regular and variable bin sizes, and including the values for the differential informature. A unimodal example in (a), and a bimodal example in (b).

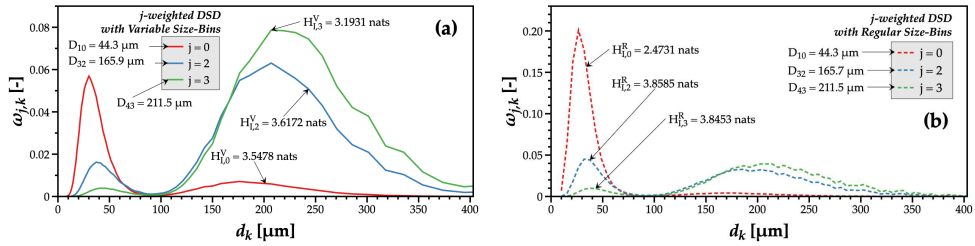


Fig. 4 Example of the number($j = 0$)-, area($j = 2$)-, and volume($j = 3$)-weighted form of a bimodal Droplet Size Distribution, using all variable (a) and regular (b) bins. The plots also include information on both mean diameter and informature values ($H^V_{I,j}$ and $H^R_{I,j}$).

Fig. 4(a), obtained with the variable bin measurement alphabet, shows the number- and volume-weighted DSDn with pronounced peaks for the smallest and largest droplets, respectively. Their informature values are therefore lower than that of the area-weighted distribution, where the size carrying the information of the spray area is more scattered in the relative frequency ω_j spectrum (d_k). With the regular bin alphabet, in Fig. 4(b), the scale and shape of the smaller droplet range remain similar to those obtained with variable bins, but the differences between the representations in the larger droplet spectrum are less pronounced. However, the same pattern remained regarding the differences in the informature values, although the gap between the area- and volume-weighted droplet size distributions closed. In all the distributions shown thus far, only when the weight changes, does one observe a change in the value of the mean diameter. However, the mean diameter of the number-, area-, or volume-weighted DSDn is blind to the changes induced by the measurement alphabet used in the calculation. At this point, we began developing a *Representation Index*, $R_{(j)}$, to help characterize the spray from an informational perspective using the differences produced by regular and variable size classes. The aim of this index is to develop an informational tool that discerns how the information on the spray density ($j = 0$), interfacial area ($j = 2$), and spray mass ($j = 3$), all present in the information acquired of drop sizes, is distributed across scales. This is analogous to the Red-Green-Blue (RGB) subpixels in a screen pixel, where the relative intensity of each fundamental color sets the tone of the pixel.

The rationale is the following. A regular alphabet partitions the size range additively, on a D scale, whereas a variable alphabet partitions it multiplicatively, on a $\ln(D)$ scale. The two partitions therefore resolve sizes differently: below a certain diameter the variable classes are finer, and above it the regular classes are. The fraction of classes activated by a given kind of information then depends on the alphabet according to the scale at which that information resides, so that the disagreement between measurement alphabets is not an artefact to be removed, but a measurable signature of where the information is located on the size scale. As shown below, this location is the j-weighted geometric mean diameter, and the reference against which it is measured is a diameter set by the measurement domain. When different kinds of information reside at different scales, their Representation Indices differ, and this difference reveals scale separation.

The first step in the development of the Representation Index is to relate the number of classes effectively carrying the spray diversity from a weighted perspective using a certain measurement alphabet (MA≡(R)egular/(V)ariable) with the total number given by Eq. (8), which we designate as an "Activation Factor"

$$\phi_j^{(MA)} = \frac{k_{eff,j}}{k} \tag{9}$$

with $\phi_j^{(R)}, \phi_j^{(V)} \in [0,1]$. Because the alphabet spans the measurement domain of the technique, $\phi_j^{(MA)}$ is the fraction of its classes effectively activated by the spray, and $-\ln \phi_j^{(MA)} = \ln k - H_{I,j}$ is the part of the information capacity of the technique left unused by carrier j. A second step then establishes the requirements for formulating a Representation Index $R_{(j)}$:

1. Symmetry – $R_{(j)}\left(\phi_j^{(R)}, \phi_j^{(V)}\right) = R_{(j)}\left(\phi_j^{(V)}, \phi_j^{(R)}\right)$
2. Normalization – for equal activation factors: $R_{(j)}(\phi, \phi) = 1$
3. Monotonic discrepancy – as $\phi_j^{(R)}$ departs from $\phi_j^{(V)}$, $R_{(j)}\left(\phi_j^{(R)}, \phi_j^{(V)}\right)$ decreases
4. Scale invariance – $R_{(j)}\left(c \cdot \phi_j^{(R)}, c \cdot \phi_j^{(V)}\right) = R_{(j)}\left(\phi_j^{(R)}, \phi_j^{(V)}\right)$ for $c > 0$

The ratio between Activation Factors, $\rho_j = \phi_j^{(V)}/\phi_j^{(R)}$, is the simplest way to relate the two measurement alphabets. To fulfil the requirements above, this relation is linearized as $\eta_j = \ln(\rho_j)$, and symmetry is ensured by taking its absolute value, $R_{(j)} = f(|\eta_j|)$. If $\phi_j^{(V)} = \phi_j^{(R)}$, then $|\eta_j| = 0$ and the Representation Index must equal unity. The simplest functional form that satisfies all four requirements is therefore

$$R_{(j)} = \exp(-|\eta_j|) \tag{10}$$

The Representation Index quantifies the invariance of the Activation Factor $\phi_j^{(MA)}$ associated with a given kind of information, under changes in the measurement alphabet used to characterize the spray. It is noteworthy that $R_{(j)} \in [0,1]$. This index

approaches unity when both measurement alphabets yield the same Activation Factor, that is, when they represent the active size range equivalently. As shown below, this neither requires a single population of droplets nor is guaranteed by one.

Because the number of classes k in Eq. (8) depends on the number of interlaced Fibonacci series J, one may ask whether $R_{(j)}$ inherits this dependence. A careful understanding of this index shows it is not. Both alphabets share the same k over the same size range, so that $\rho_j = \phi_j^{(V)}/\phi_j^{(R)} = k_{eff,j}^{(V)}/k_{eff,j}^{(R)}$ and k cancels. Since $k_{eff,j} = \exp(H_{I,j})$ in both alphabets, $\eta_j = H_{I,j}^{(V)} - H_{I,j}^{(R)}$ exactly. Writing the informature of each alphabet through Eq. (6), and recalling that the differential informature is essentially independent of the measurement alphabet, η_j reduces to the difference between the two grid terms, $G_j^{(R)} - G_j^{(V)}$. Regular classes have a constant width $(D_{max} - D_{min})/k$, whereas variable classes have a width proportional to their centre, approximately $d_i \ln(D_{max}/D_{min})/k$, where d_i is the class centroid. Therefore, the two widths coincide at a crossover diameter

$$D_\times = \frac{D_{max} - D_{min}}{\ln\left(D_{max}/D_{min}\right)}, \tag{11}$$

which is the logarithmic mean of the size-range limits. Retaining the leading term of an exact expression for η_j (Appendix A), the Representation Index becomes

$$R_{(j)} \simeq \exp\left(-\left|\ln\frac{D_\times}{D_{g,j}}\right|\right), \tag{12}$$

where $D_{g,j} = \exp\left(\sum_i \omega_{j,i}^{(V)} \ln d_i^{(V)}\right)$ is the geometric mean diameter of the j-weighted DSDn, evaluated with the relative frequencies $\omega_{j,i}^{(V)}$ and class centres $d_i^{(V)}$ of the variable measurement alphabet. It enters through the grid term of that alphabet, $G_j^{(V)}$, whose class widths are proportional to their centres, and it tends to the geometric mean of the droplet sample as the classes are refined. The number of classes, and therefore J, no longer appears. From the raw data, this geometric mean diameter can also be calculated as $D_{g,j} = \exp\left(\sum_n D_n^j \ln D_n / \sum_n D_n^j\right)$, where D_n is the diameter of each droplet.

The route to Eq. (12) is itself infodynamic, and it is worth making explicit. It rests on the distinction introduced in Sec. 2 between the informature, an extensive quantity that depends on the measurement alphabet, and the differential informature, an intensive quantity that does not. Eq. (6) splits the former into the latter and the grid term G_j. The differential informature is a property of the spray, the same whichever alphabet is used to measure it, so it cancels when the two alphabets are compared through η_j. What remains is the difference between their grid terms, $G_j^{(R)} - G_j^{(V)}$, that is, between the information that each alphabet adds through the widths of its classes. In a regular alphabet, all classes have the same width, and $G_j^{(R)}$ is a constant. However, in a variable alphabet, the class widths grow in proportion to their centres, and $G_j^{(V)}$ is the logarithm of the geometric mean diameter, $\ln D_{g,j}$, plus a constant (Appendix A). $D_{g,j}$ and $D_\times$ are therefore not statistical descriptors appended to the index from outside, but the form assumed by the extensive part of the informature once its intensive part has been removed. Without the distinction between extensive

and intensive informature, nothing would suggest comparing $D_{g,j}$ with the logarithmic mean of the size range, and with it, the comparison follows directly. Eq. (12) does not replace the informational construction of $R_{(j)}$ because it is its result, and $D_\times$ acquires a precise informational meaning as the scale at which the two partitions of the size range contribute the same grid information.

Eq. (12) also gives the Representation Index a direct physical reading. $R_{(j)}$ approaches unity when the j-weighted population is centred, on a logarithmic scale, on the diameter at which both alphabets resolve sizes equally, $D_\times$, and it decreases as that population moves towards scales where one alphabet resolves sizes more finely than the other. In terms of information carriers, $R_{(j)} \to 1$ means that the information carried by j is represented equally by both partitions of the size scale, so that its description does not depend on the partition chosen by the observer.

To illustrate how the Representation Index should be read, Fig. 5(a) shows four distributions based on the log-normal: the unimodal and bimodal distributions of this section, and two further cases built to test the interpretation of the index, a narrow population at 20 μm and two equally weighted narrow populations at 20 and 224 μm. Fig. 5(b) shows the two class widths for the PDI configuration of this work ($D_{min} = 1$ μm, $D_{max} = 403$ μm, $k = 112$), which coincide at $D_\times = 67$ μm, the reference scale of the measurement.

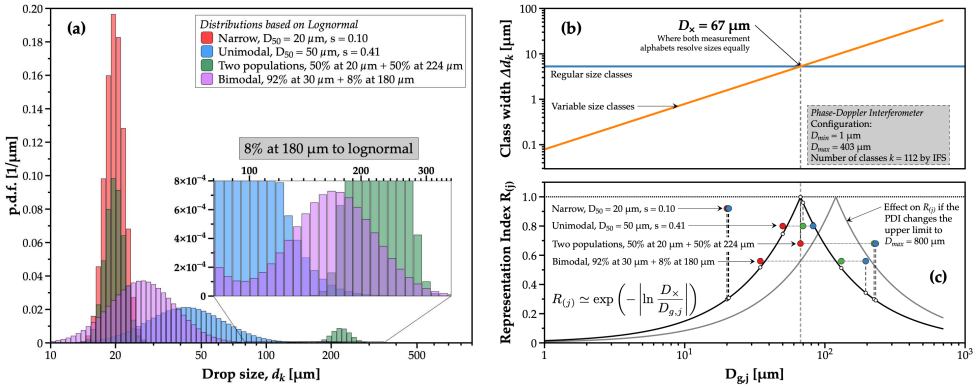


Fig. 5 (a) Probability density of the four log-normal-based distributions, built with the variable alphabet of the PDI instrument; the inset magnifies the 8% population at 180 μm of the bimodal case. (b) Class width of the regular and variable alphabets of the PDI instrument ($D_{min} = 1$ μm, $D_{max} = 403$ μm, $k = 112$), equal at $D_\times = 67$ μm, Eq. (11). (c) $R_{(j)}$ from Eq. (12) versus $D_{g,j}$, with the number (red), area (blue), and volume (green) carriers of the distributions in (a), drawn at arbitrary heights and projected onto the curve; grey line: $D_{max} = 800$ μm ($D_\times \approx 120$ μm).

Fig. 5(c) gives the corresponding reading of Eq. (12). $R_{(j)}$ equals one when $D_{g,j} = D_\times$ and decreases symmetrically, on a logarithmic scale, as $D_{g,j}$ moves away from $D_\times$ in either direction. The figure places on this curve the three carriers of each distribution in Fig. 5(a). The ordering $D_{g,0} \le D_{g,2} \le D_{g,3}$ always holds, because $\mathrm{d}\ln D_{g,j}/\mathrm{d}j = \mathrm{Var}_j(\ln D) \ge 0$, the variance of $\ln D$ under the j-weighted distribution. On the logarithmic axis of Fig. 5(c), the carriers of each spray therefore lie

between $D_{g,0}$ and $D_{g,3}$. These two diameters are not two statistics of the same distribution, but the centres of two different distributions built from the same droplets, one weighted by number and the other by volume. The distance between them, $\ln(D_{g,3}/D_{g,0}) = \int_0^3 \mathrm{Var}_j(\ln D)\,\mathrm{d}j$, measures how far apart, on a logarithmic scale, the sizes that carry the number of droplets and those that carry their volume lie. It is zero for a monodisperse spray, grows with the diversity of droplet sizes, and equals $3s^2$ for a log-normal DSDn, whose j-weighted forms are all log-normal with the same s.

Two consequences follow, and both are needed to interpret $R_{(j)}$ correctly. First, the Representation Index of a single carrier does not, by itself, distinguish one population from several. The narrow population at 20 μm yields $R_{(0)} = 0.30$, which is far from unity because its scale lies far below $D_\times$, whereas the two populations at 20 and 224 μm yield $R_{(0)} \simeq 1.00$ because the number-weighted geometric mean of the mixture, 67 μm, happens to coincide with $D_\times$, although no droplet has that size. A single $R_{(j)}$ locates carrier j relative to the reference scale of the measurement, although this is not a test of coherence on its own. Second, scale separation is revealed by the differences between carriers. In the narrow population, the three carriers coincide, $R_{\{(0),(2),(3)\}} = 0.30,\ 0.30,\ 0.31$, which identifies a single coherent scale, even if it is poorly centred in the alphabet. In the two populations, the number carrier sits at 67 μm, whereas the area and volume carriers sit at 224 and 230 μm, and $R_{\{(0),(2),(3)\}} = \{1.00,\ 0.30,\ 0.29\}$, meaning the information on the spray density and the information on its interfacial area and mass reside at separated scales. This is why the spread of $R_{(j)}$ across j, and the combined indices introduced below, are the appropriate measures of multi-carrier coherence.

The Representation Index also depends on the configuration of the instrument, since $D_\times$ is set by the measurement domain. For the same spray measured with $D_{max} = 800$ μm, $D_\times \approx 120$ μm, and the curve in Fig. 5(c) shifts to the right (grey line), changing every single $R_{(j)}$. The carriers of the spray do not move, only the reference does. Therefore, values of $R_{(j)}$ are directly comparable only when computed over the same measurement domain, which must be reported, and all the examples of this work, simulated or measured, use the PDI domain. Because this domain is known before the measurement, $R_{(j)}$ can also be evaluated at each point during the acquisition. This dependence on the instrument also suggests a use of the index beyond characterization. When the carriers of a spray are far from $D_\times$, as in the narrow population case, most of the size range of the configuration includes sizes that the spray does not produce, and the regular alphabet, whose constant class width resembles the approximately constant absolute size resolution of phase-Doppler sizing, resolves that spray poorly.

For an optical configuration that can be adapted, $R_{(j)}$ could therefore guide the choice of the size range. If the size range is chosen so that $D_\times$ coincides with the geometric centre of the carriers, $\sqrt{D_{g,0}D_{g,3}}$, estimated from a preliminary measurement, the number and volume carriers lie at the same logarithmic distance on either side of $D_\times$, so that $R_{(0)} = R_{(3)} = \sqrt{D_{g,0}/D_{g,3}}$, and $R_{(2)}$, which lies between them, is higher. Any other choice brings $D_\times$ closer to one carrier and further from the other, lowering the smaller of the two indices. The part of $R_{(j)}$ that then remains below unity no longer reflects the measurement domain, but the diversity of droplet sizes of the spray

itself, which no choice of size range can remove, as quantified below by Eq. (13). Conceptually, the reference could instead be placed on the carrier most relevant to the application, for example $D_\times = D_{g,2}$, so that $R_{(2)} = 1$, when interfacial processes such as evaporation or gas absorption are of interest. In phase-Doppler systems, a smaller size range is obtained, for example, with shorter focal lengths, which also reduce the probe volume and the probability of multiple droplet occupancy in dense sprays. Such an adaptation must, however, be made once, before a measurement campaign, since values of $R_{(j)}$ remain comparable only when computed over a common measurement domain.

Eq. (10) and Eq. (12) are two ways of computing the same index, not two different representations. Eq. (10) counts the classes effectively activated in each alphabet from the binned data, whereas Eq. (12) is its closed form, derived in Appendix A, and requires only $D_{g,j}$ and $D_\times$. For the simulated distributions of this section, the largest absolute difference between $R_{(j)}$ computed from Eq. (10) and from Eq. (12) is 0.008 for the single indices and 0.011 for the combined ones with the $J = 3$ alphabet used here (Fig. 6), and at most 0.011 for the single indices with $2 \leq J \leq 6$, and the ordering of the information carriers is preserved throughout. Because it involves only a weighted mean of $\ln d$, Eq. (12) can also be evaluated droplet by droplet, without any measurement alphabet or dependence on J. This is how $R_{(j)}$ is computed for the PDI measurements in Sec. 5, where some positions contain only a few hundred droplets and the two informature estimates required by Eq. (10) become unreliable.

This formulation also allows the combined effect of two independent Activation Factors to be evaluated. Because $R_{(j)} = \exp(-|\eta_j|)$, independent contributions are additive in η_j and therefore multiplicative in $R_{(j)}$, which is a further reason for linearizing the ratio of Activation Factors logarithmically. For example, if we consider the coupling of the information of spray density given by the number-weighted ($j = 0$) and the information on the spray interfacial area given by the area-weighted ($j = 2$) perspective, the outcome is readily shown to be the product of the Representation Index of each j-weighted distribution, *e.g.*, $R(\eta_0, \eta_2) = R_{(0,2)} = R_{(0)} \cdot R_{(2)}$. Combined indices also recover a part of the information that is independent of the instrument. When two carriers lie on opposite sides of $D_\times$, for example $D_{g,0} < D_\times < D_{g,3}$, their combined index is $R_{(0)}R_{(3)} = (D_{g,0}/D_\times)(D_\times/D_{g,3}) = D_{g,0}/D_{g,3}$, and $D_\times$ cancels. Integrating $\mathrm{d}\ln D_{g,j}/\mathrm{d}j = \mathrm{Var}_j(\ln D)$,

$$R_{(0)}R_{(3)} = \frac{D_{g,0}}{D_{g,3}} = \exp\left(-\int_0^3 \mathrm{Var}_j(\ln D)\,\mathrm{d}j\right), \tag{13}$$

which measures the logarithmic distance between the scales at which the information on number and on volume resides. For a log-normal distribution, $\mathrm{Var}_j(\ln D) = s^2$ for every j, and Eq. (13) gives $\exp(-3s^2)$, that is, 0.607 for the unimodal distribution of this section ($s^2 = 1/6$), against 0.605 computed from the simulated droplets. This invariance holds as long as $D_\times$ remains between the two carriers. When both lie on the same side, as in the narrow population, the combined index again depends on the measurement domain. Fig. 6 shows the Representation Index for single j-weighted DSDn and for combined cases, for both the simulated unimodal and bimodal drop size distributions.

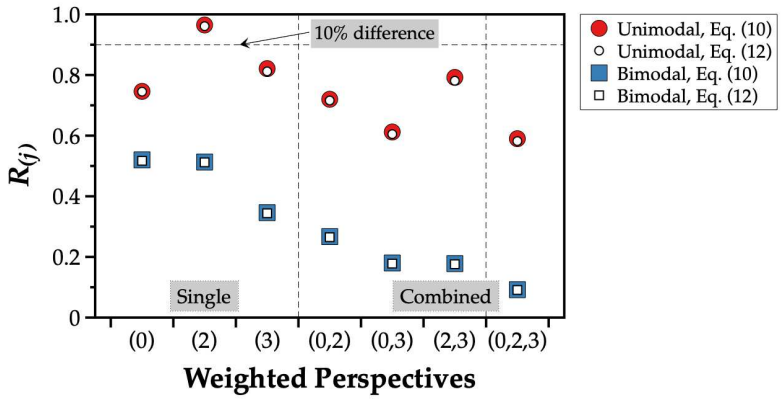


Fig. 6 Representation Index $R_{(j)}$, single and combined, for the simulated unimodal and bimodal distributions, computed with Eq. (10) (filled symbols) and Eq. (12) (open symbols), with the measurement alphabet of the PDI instrument.

Differences in $R_{(j)}$ across j reveal how the information carried by number (fine droplets), interfacial area, and volume (mass) is distributed across scales, as anticipated in Fig. 5(c). In the unimodal case, the three carriers lie close to each other around $D_\times$. The area carrier ($D_{g,2} = 69.7$ μm) nearly coincides with it, $R_{(2)} = 0.96$, while the number ($D_{g,0} = 49.9$ μm) and volume ($D_{g,3} = 82.5$ μm) carriers lie slightly below and above it, with $R_{(0)} = 0.74$ and $R_{(3)} = 0.81$. The spread of the single indices is moderate, and the combined index $R_{(0,2,3)} = 0.58$ indicates that the three kinds of information are carried by a common band of scales.

In the bimodal case, the droplet size distribution is composed of two distinct clusters by construction: a dominant (92%) cluster of smaller droplets and a minor (8%) cluster of larger ones. The number carrier remains in the cluster of small droplets, $D_{g,0} = 34.7$ μm, below $D_\times$, whereas the area and volume carriers move to the cluster of large droplets, $D_{g,2} = 131$ μm and $D_{g,3} = 195$ μm, above $D_\times$. Although the single indices of the number and area carriers are similar, $R_{(0)} = 0.52$ and $R_{(2)} = 0.51$, they arise on opposite sides of $D_\times$, which is precisely the separation of scales that the combined indices expose. Because the number and volume carriers lie below and above $D_\times$, respectively, Eq. (13) gives $R_{(0,3)} = D_{g,0}/D_{g,3} = 0.18$, against 0.60 in the unimodal case, a ratio independent of the instrument that measures how far apart, on a logarithmic scale, the information on the spray density and on the spray mass resides.

The combined indices $R_{(0,2)}$, $R_{(0,3)}$, and $R_{(0,2,3)}$ quantify the multi-carrier coherence. Their collapse in the bimodal case, $R_{(0,2,3)} = 0.09$ against 0.58 in the unimodal case, demonstrates that no single alphabet yields a consistent informational description across the spray density (number-induced), interfacial area (area-induced), and mass (volume-induced) informational views. This is a quantitative signature both of carrier switching as j changes and of scale separation, since the regions of the droplet spectrum that carry a particular informational aspect of the spray lie at different scales. There is no right or wrong measurement alphabet for representing drop sizes. However, their differences, read through $D_{g,j}$ and $D_\times$, identify where each kind of information resides and, through the spread of $R_{(j)}$ across j and the combined indices,

whether different kinds of information reside at separated scales. This analysis provides a basis for interpreting the experimental infodynamic signatures discussed in the following sections. The next section presents the experimental setup and diagnostic techniques that allowed us to perform the infodynamic characterization of effervescent sprays.

4 Experimental Setup and Diagnostic Technique

A single-orifice effervescent atomizer was tested in this study at a constant injection overpressure of 100 kPa for several GLRs ranging from 2.5 to 10%. Water and air were mixed inside a mixing chamber with a diameter of 15 mm. Air was injected into the mixing chamber through 64 aerator orifices, each with a diameter of 0.6 mm. The resulting two-phase flow was then discharged through an exit orifice with a diameter of $d_o = 1.2$ mm. A schematic representation of the atomizer is shown in Fig. 7.

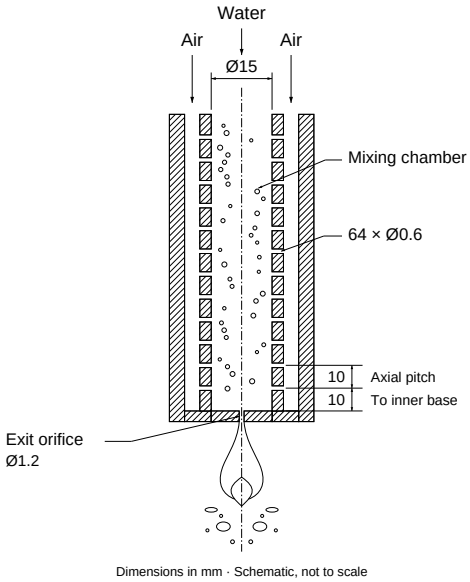


Fig. 7 Schematic layout of the effervescent atomizer (adapted from Cejpek et al. (2023a)).

Water was pumped from the storage tank to the atomizer using a gear pump. The water flow rate was measured using a Coriolis mass flow meter (Mass 2100 Di3) fitted with a Mass 6000 transmitter (Siemens AG., GE), with an accuracy of ±0.1% of the actual flow rate. The inlet pressures of the water and atomization gas were measured using piezoresistive pressure sensors (BD Sensor DMP 331i, BD SENSORS s.r.o., CZ), with a measurement accuracy of ±2 kPa. The atomization air flow rate was measured using an FMA–A2100 mass flow meter (Omega Engineering, USA), with an accuracy of ±1% of the actual flow rate.

The water flow rates were 19.9, 15.3 and 10.4 kg/h and the air flow rates 0.51, 0.75 and 1.02 kg/h for GLR $\simeq$ 2.5, 5 and 10%. Bubbly flow is excluded at all three conditions, since it requires GLR $\leq 4.6\,\rho_g/\rho_l$, with ρ_g the air density in the mixing chamber, that is, GLR $\lesssim$ 1.2% at this pressure (Jedelský and Jicha 2013), and the superficial gas velocity in the exit orifice, 50, 74 and 100 m/s, exceeds by five to ten times the transition to annular flow in vertical tubes, about 10 m/s (Taitel et al. 1980). The three conditions are therefore treated as one regime of annular discharge, and the effect of GLR is examined within it. Near the exit orifice, the spray has a similar morphology at the three GLRs (Fig. 8): a dense liquid core that disintegrates into a dispersed spray cone.

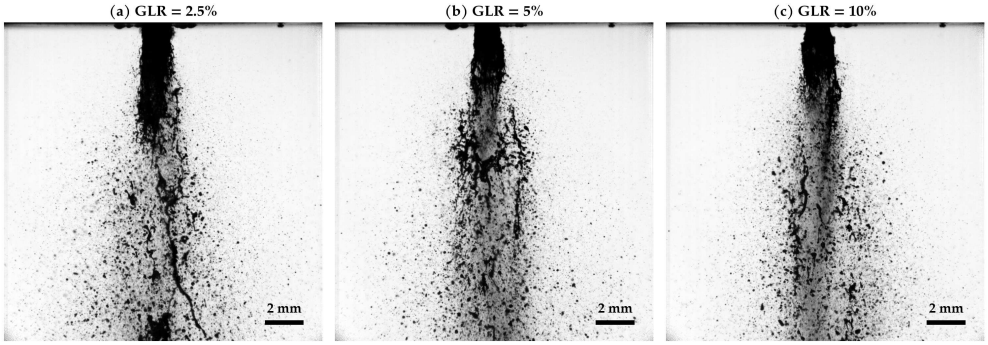


Fig. 8 Near-nozzle spray at an injection overpressure of 100 kPa for (a) GLR = 2.5%, (b) 5% and (c) 10%: single frames of backlit high-speed recordings, at 16 µm per pixel (Cejpek et al. 2023a). The exit orifice is at the top of each frame.

Droplet sizes and velocities were acquired using a two-component fiber-based Phase Doppler Interferometry (PDI) measurement system (Dantec Dynamics A/S, Skovlunde, Denmark). Non-coincident two-component velocity measurements were performed simultaneously with droplet sizing. Several points along two perpendicular axes were probed at an axial distance of $z = 100$ mm from the atomizer tip. Either 35 000 samples were acquired, or a 30 s acquisition duration was reached, whichever occurred first. However, using the infodynamic criterion of the temporal stabilization of the differential informature, $dH_{\Delta,j}/dt \approx 0$ (Ferrão et al. 2025), all points fulfilled the criterion, including those with the lowest number of data samples. Dantec BSA software version 5.2 was used to control the measurement location and data acquisition criteria. The PDI settings are summarized in Table 1. The PDI configuration and acquisition protocol followed the diagnostic approach previously used by Cejpek et al. (2023a) for effervescent atomizer spray measurements.

5 Characterization of Effervescent Sprays

This section presents the results. Sec. 5.1 describes the spray through its conventional physical characteristics, the mean diameters and the mean and fluctuating droplet

Table 1 PDI setup parameters.

Parameter	Value
Laser power output	350 mW
Scattering angle	72°
Receiver mask	C
Receiver spatial filter	0.2 mm
Focal length (transmitting/receiving optics)	500/500 mm
Wavelengths	488 nm, 514.5 nm
Velocity components	Axial, Radial
Velocity centre	25.7 m/s, 0 m/s
Velocity span	51.4 m/s, 24.4 m/s
Sensitivity	950 V, 1080 V
Signal-to-noise ratio	0 dB, 0 dB
Signal gain	8 dB, 10 dB
Level validation ratio	8

velocities, and assesses its symmetry. Secs. 5.2 and 5.3 present the two infodynamic patterns obtained from the quantification of drop size diversity, and Sec. 5.4 interprets them through a local Stokes number analysis. First, we clarify how we processed the data to build the measurement alphabets.

The PDI technique has a limitation when measuring droplet sizes below 1 μm because these approach the scale of the laser beam wavelength. The lower limit of the measurement domain is therefore $D_{min} = D_0 = 1$ μm, the lower edge of the geometric progression of the variable alphabet, whose edges are $D_l = D_0 \cdot SR^{l/k}$, $l = 1, \ldots, k$; the few droplets validated below 1 μm, if any, are assigned to the first class. With regular size classes, we divide the size range by the number of k classes. In both alphabets, the number of classes follows from Eq. (8) with $J = 3$ interlaced Fibonacci series, which gives $k = 112$ over the PDI measurement domain. The upper edge of both alphabets is the maximum diameter allowed by the PDI configuration, $D_{max} \approx 403$ μm, independently of the largest droplet recorded at each position (see Sec. 3).

The measurement grid points were on the $(x, 0)$ and $(0, y)$-axes from -25 mm : $\Delta x = \Delta y = 2.5$ mm : 25 mm, corresponding to 42 measurement points in the three GLR (2.5%, 5%, 10%) conditions. Both alphabets were built once over this measurement domain and used at every position and GLR condition to perform the informational characterization of the spray's radial profile. These measurement alphabets affect only the infodynamic characteristics of the spray, except for the differential informature given by Eq. (6). We begin with the physical characteristics of the spray and its symmetry.

5.1 Spray characteristics

Fig. 9 presents the characteristics of the spray droplets along the $(x, 0)$ and $(0, y)$ traverses for the three GLR conditions: the number-, area- and volume-weighted mean diameters, D_{10}, D_{32} and D_{43}, and the mean axial velocity of the droplets, $\bar{u}$, with its root-mean-square fluctuation, u_{RMS}, computed from all validated droplets at each measurement point.

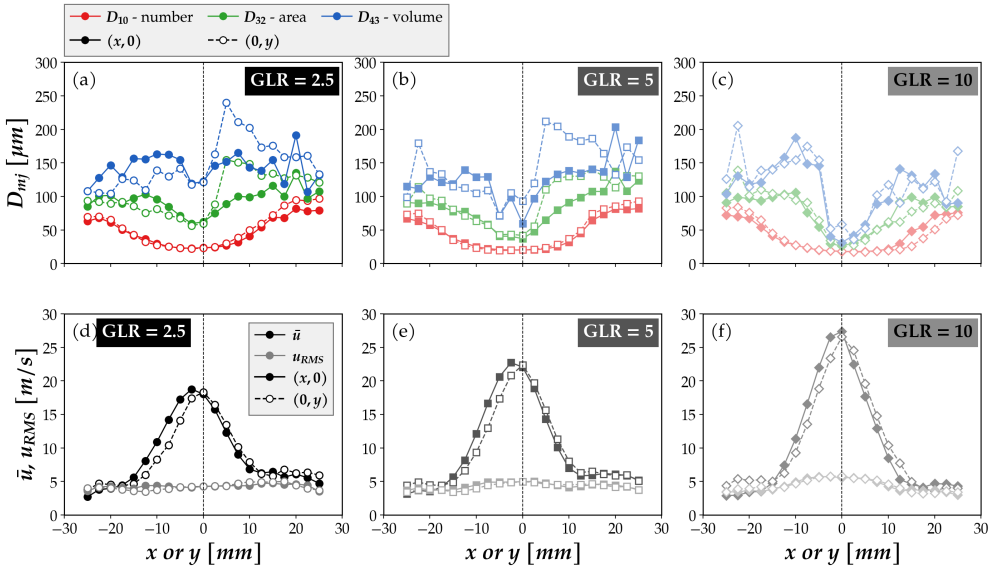


Fig. 9 Physical characteristics of the effervescent spray at $z = 100$ mm along the $(x, 0)$ (filled symbols, solid lines) and $(0, y)$ (open symbols, dashed lines) traverses for GLR = 2.5, 5 and 10%: (a–c) number-, area- and volume-weighted mean diameters, D_{10}, D_{32} and D_{43}; (d–f) mean axial droplet velocity, $\bar{u}$, and its root-mean-square fluctuation, u_{RMS}. Circles, squares and diamonds: GLR = 2.5, 5 and 10%.

Increasing the GLR at constant injection pressure lowers the liquid flow rate and raises the gas flow rate, so that the two-phase mixture leaves the exit orifice faster. The mean axial droplet velocity on the spray axis increases accordingly, from 18 to 22 and 27 m/s for GLR = 2.5, 5 and 10%, close to the local gas velocity (more details in Sec. 5.4), which indicates that the droplets on the axis are essentially carried by the gas. The width of the velocity profile, however, remains nearly the same, so that the GLR accelerates the jet without widening it. The mean diameters respond differently to the GLR depending on the weighting. D_{10}, dominated by the numerous small droplets, changes little on the axis, whereas D_{32} and D_{43} decrease markedly, which means that the GLR removes the large droplets from the spray core rather than producing smaller droplets overall. In the periphery, the mean diameters are similar for the three conditions, so that the radial contrast between a fine core and a coarse periphery increases with the GLR. The velocity fluctuation adds a further piece of information. On the axis, u_{RMS} is about 20% of $\bar{u}$, as in a turbulent jet, but towards the periphery it becomes comparable to $\bar{u}$ itself, too large to be attributed to the gas turbulence alone. This indicates that droplets with very different velocities coexist there, slow droplets that follow the decelerating gas and faster ones that arrive on their own inertia, a coexistence that the infodynamic analysis of Sec. 5.2 quantifies directly from the size distribution.

Fig. 10 evaluates the symmetry of the effervescent spray by comparing the $(x, 0)$ and $(0, y)$ radial profiles for the three mean diameters (number-, area-, and volume-weighted), and the three differential informatures (information of spray density, interfacial area, mass) under three distinct GLR (2.5%, 5%, and 10%) conditions. The results show that the spray was relatively symmetric, although asymmetries were accentuated for higher j-weights. However, in the case of the spray differential informature, these asymmetries appeared to be less pronounced. Asymmetry in the physical characteristics of the spray was present across all three GLR conditions and showed no systematic trend with increasing GLR, suggesting that it was related to the atomizer geometry or mounting rather than to the internal flow.

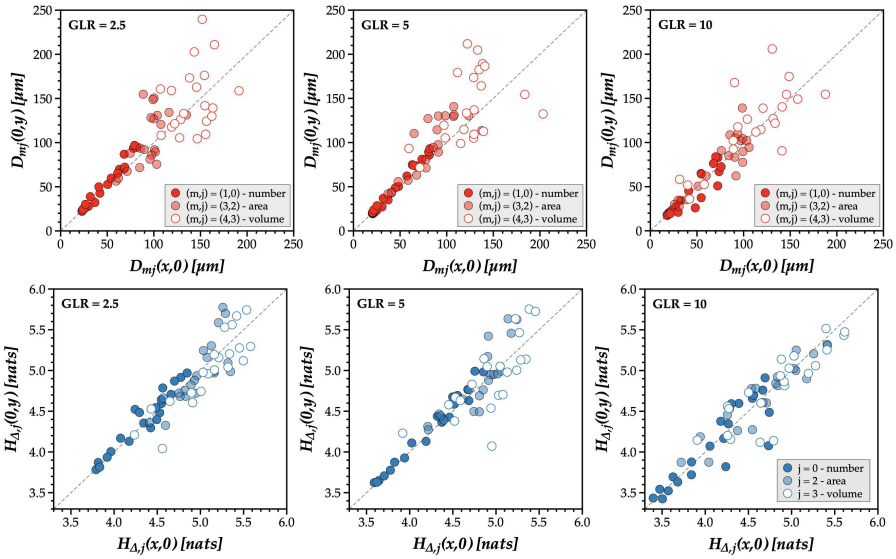


Fig. 10 Symmetry of the spray from the mean diameter D_{mj} (with $m = j + 1$) on top, and below from the differential informature $H_{\Delta,j}$ perspective for the GLR of 2.5, 5 and 10%.

5.2 First infodynamic pattern: an info-hollow-cone spray

The radial profiles of the differential informature exemplified for the number-weighted drop size distribution in Fig. 11 for GLR = 10% show, for the first time an infodynamic pattern: the spray informational structure as an *info-hollow-cone spray*.

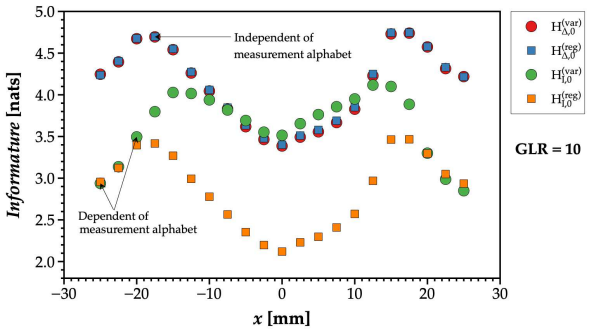


Fig. 11 Comparing the role of the measurement alphabet (○ - variable; □ - regular) in informature and differential informature.

While the differential informature ($H_{\Delta,0}$) for the number-weighted drop size distribution is independent of the measurement alphabet, informature ($H_{I,0}$) is sensitive to the regularity or variability of size classes. Therefore, the informational structure characteristics of the spray rely on differential informature (an intensive property of the physical system such as temperature). The local values of the differential informature express the amount of information required to determine the diversity of drop sizes. This diversity exhibited a local peak at the location where we expected the interface region between the spray and the environment, for the three GLR conditions and the three j-weights (Fig. 13).

In Cejpek et al. (2023a), the spray cone angles (SCA) obtained from high-speed imaging were between $20° - 30°$, and using the number-weighted differential informature, the SCA was approximately 20°. The SCA boundary corresponds to the radial position enclosing approximately 90% of the cumulative droplet volume, located at a radius of 17–20 mm. This agreement indicates that the differential informature peak is consistent with the location of the spray/ambient interface from the droplet size distribution alone. Physically, this interface is the outer edge of the gas jet, where two populations of droplets coexist: droplets that move with the decelerated gas, at 1–4 m/s, mostly smaller than 70 μm, and droplets larger than 70 μm that still move at 6–16 m/s, three to six times faster, and therefore reach this region on their own inertia rather than carried by the gas, as the Stokes number analysis of Sec. 5.4 confirms. To see how this coexistence enters the differential informature, the droplets at each point where the local gas velocity U_G could be estimated (Sec. 5.4 and Appendix B) were split into an inertial population, moving faster than $2U_G$, with number fraction ζ_1, and a gas-carried population, with $\zeta_2 = 1 - \zeta_1$. Because both populations share the same variable classes, $H_{\Delta,0}$ separates exactly as

$$H_{\Delta,0} = \zeta_1 H^{(1)}_{\Delta,0} + \zeta_2 H^{(2)}_{\Delta,0} + D_{JS}, \tag{14}$$

where $H^{(k)}_{\Delta,0}$ is the differential informature of population k, and D_{JS}, the generalized Jensen–Shannon divergence between the two size distributions (Lin 1991), is the diversity added by their coexistence: it is zero when both populations have the

same size distribution and reaches $-\zeta_1 \ln \zeta_1 - \zeta_2 \ln \zeta_2$ when they occupy disjoint size ranges (Appendix B). Fig. 12(a–c) shows this decomposition along the $(x, 0)$ traverse at GLR= 10%. On the axis, all droplets move with the gas, and $D_{JS} = 0$. Mid-way, one droplet in five is inertial, mostly among the larger sizes, and $D_{JS} = 0.079$ nats. At the informature peak, the two populations have comparable weights, the inertial droplets dominate above 60 μm, and $D_{JS} = 0.175$ nats. For all GLRs, D_{JS} is negligible within 7.5 mm of the axis and grows with $H_{\Delta,0}$ up to its peak, where it accounts for 11–31% of the increase from the axis (Fig. 12d–f). The remainder comes from the first two terms of Eq. (14), because each population also widens and shifts to larger sizes. D_{JS} reaches only 21–42% of its maximum, because inertial droplets are also found among the small sizes: the two populations are separated more sharply by velocity than by size. The $H_{\Delta,0}$ peak is therefore where the coexistence of gas-carried and inertial droplets contributes most to the diversity of sizes, although it is not its only source. Beyond the peak, U_G could not be estimated, and the decomposition is limited to the region up to it.

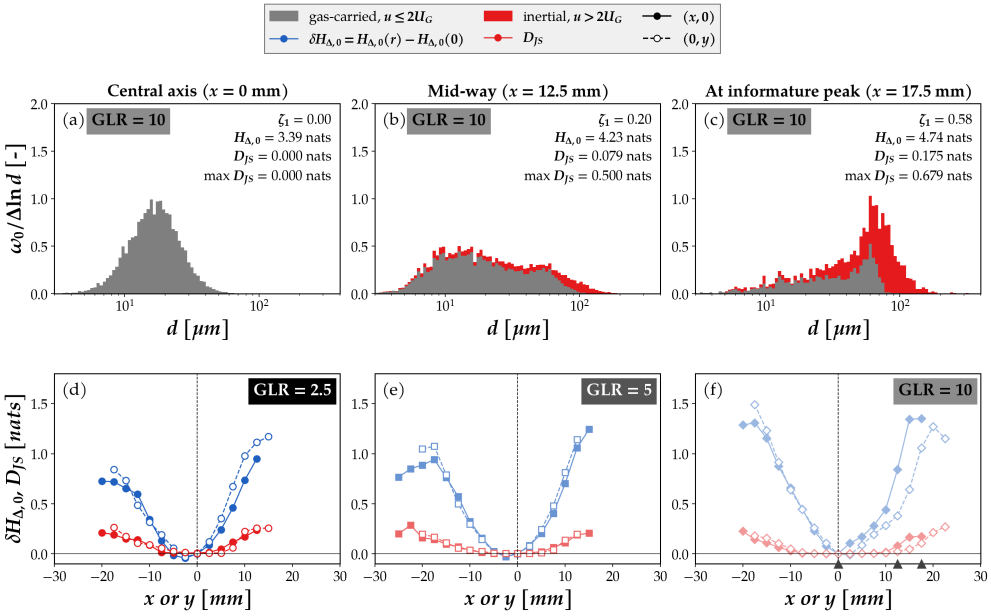


Fig. 12 Number-weighted size distribution per logarithmic class width along the $(x, 0)$ traverse at GLR = 10%, (a) on the axis, (b) mid-way and (c) at the $H_{\Delta,0}$ peak, split into gas-carried ($u \leq 2U_G$, grey) and inertial ($u > 2U_G$, red) droplets, with ζ_1 the number fraction of inertial droplets; (d–f) increase of $H_{\Delta,0}$ from its value on the axis, $\delta H_{\Delta,0}$, and coexistence term D_{JS} of Eq. (14), at the points where U_G could be estimated. Triangles in (f) mark the locations of (a–c).

The rest follows from Eq. (6), $H_{\Delta,0} = H_{I,0}^{(V)} + G_0^{(V)}$. With variable classes, whose widths are proportional to their centres, the grid term $G_0^{(V)}$ is the logarithm of the geometric mean diameter $D_{g,0}$ plus a constant (Appendix A), so that $H_{\Delta,0}$ is the sum

of $\ln k_{eff,0}^{(V)}$, the logarithm of the effective number of variable classes, which does not change when all sizes are scaled by the same factor, and $\ln D_{g,0}$, the logarithm of the size scale, plus that constant. For GLR = 10%, $k_{eff,0}^{(V)}$ grows from 34 to 61 within 12.5 mm of the axis while $D_{g,0}$ remains at 15–21 μm. Between 12.5 and 17.5 mm, $D_{g,0}$ doubles to 44 μm as the large droplets arrive, and $H_{\Delta,0}$ reaches its peak. Beyond the peak, $D_{g,0}$ grows to 73 μm, but the large droplets form a narrow population ($k_{eff,0}^{(V)} = 17$ at 25 mm), and $H_{\Delta,0}$ decreases. The $H_{\Delta,0}$ peak is thus where the diversity of sizes and the sizes it spans are jointly largest. At this distance from the nozzle, the interface gathers this diversity rather than producing it, since the Weber number of the droplets, based on their velocity relative to the local gas, remains below 3.5, well below the critical value of about 12 for secondary breakup (Guildenbecher et al. 2009).

The lowest values of $H_{\Delta,j}$ were consistently observed in the spray center, where a high-speed gas core is present and the droplet size distribution is narrow. The center is not depleted of small droplets, which make up most of the samples there, but of large ones: droplets larger than 40 μm are 10%, 5% and 2% of the droplets on the axis for GLR = 2.5, 5 and 10%, against 59–87% at the $H_{\Delta,0}$ peak. The small droplets relax to the gas velocity and are carried with the jet, whereas the large ones, weakly coupled to the gas, move on their own inertia towards the outer part of the spray. The center therefore holds a single population moving with the gas, which reduces the size diversity. The minimum is most pronounced at GLR = 10%, where the gas core is fastest ($U_{G,\text{axis}} = 17.5$, 21.3 and 26.3 m/s for GLR = 2.5, 5 and 10%, Appendix B) and the share of large droplets on the axis is smallest.

Another noteworthy feature shown in Fig. 13 is the asymmetry observed in the regions $(x > 0, 0)$ and $(0, y > 0)$ of the radial profiles with respect to the effect of GLR.

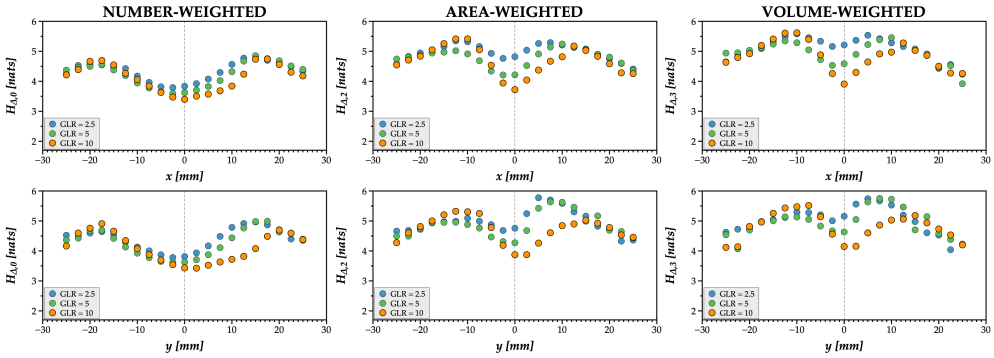


Fig. 13 Spray Informational Structure and effect of GLR on the radial profiles of the differential informature $H_{\Delta,j}$.

In all j-weights considered, we observed a loss in the amount of information needed to determine the diversity inside the info-hollow cone spray. The contribution from the PDI measurement principle should also be considered for the asymmetry observed in the regions $(x > 0, 0)$ and $(0, y > 0)$. The signal from droplets located at positive x

and y positions must travel larger distances to reach the receiving optics. This signal path intersects the dense inner spray region. Consistently lower velocity validation rates were observed for these positions, whereas the spherical validation rate remained symmetric. The maximum difference in the overall validation rate between the opposite sides was less than 6%.

The differential informature is computed from the droplet sizes alone, yet its radial profile behaves like a kinematic quantity. Fig. 14 compares $H_{\Delta,0}$ with the relative fluctuation of the axial droplet velocity, $u_{RMS}/\bar{u}$, which cannot be read as a turbulence intensity, since it mixes the turbulence of the gas with the velocity difference between droplets of different inertia, but for that very reason measures how far the droplets at one point share the same motion. From the axis to 15–17.5 mm, the two quantities rise together along every traverse and every GLR, and within that range they are nearly a single-valued function of each other (Fig. 14d–f), with correlation coefficients of 0.74, 0.83 and 0.88 for GLR = 2.5, 5 and 10%. $H_{\Delta,0}$ reaches its peak where $u_{RMS}/\bar{u}$ reaches 0.7–0.9, that is, where the velocity fluctuation becomes of the order of the mean velocity. This is the behaviour expected if both quantities respond to the same physical process: the coexistence, at the edge of the gas jet, of small droplets that have relaxed to the decelerating gas and large droplets that arrive on their own inertia. The sizes record this coexistence as diversity, while the velocities record it as dispersion. Beyond the peak, however, the two quantities separate. While $u_{RMS}/\bar{u}$ remains at 0.7–0.9, and on the negative side keeps rising to 1.0–1.3, because $\bar{u}$ falls to 3–4 m/s and a few inertial droplets suffice to make the fluctuation comparable to the mean, the points at $|r| \geq 20$ mm leave the common curve in Fig. 14(d–f). $H_{\Delta,0}$, instead, decreases, because the gas-carried population has been left behind and only the coarse, narrow population of inertial droplets remains. Therefore, the velocity fluctuation cannot distinguish a region where two populations coexist from a region where a single population moves through a slow gas, whereas the size diversity can. The two descriptions are complementary rather than competing: the dynamic characteristics locate where the droplets move with or regardless of the gas, and the informational characteristic expresses how many kinds of droplets are present at that location. A characterization based on mean sizes and velocities alone, even with their fluctuations, would place the spray boundary at the plateau of $u_{RMS}/\bar{u}$ and miss that the diversity of the spray peaks there and then decays, which is the structure that the following analysis of the Representation Index develops.

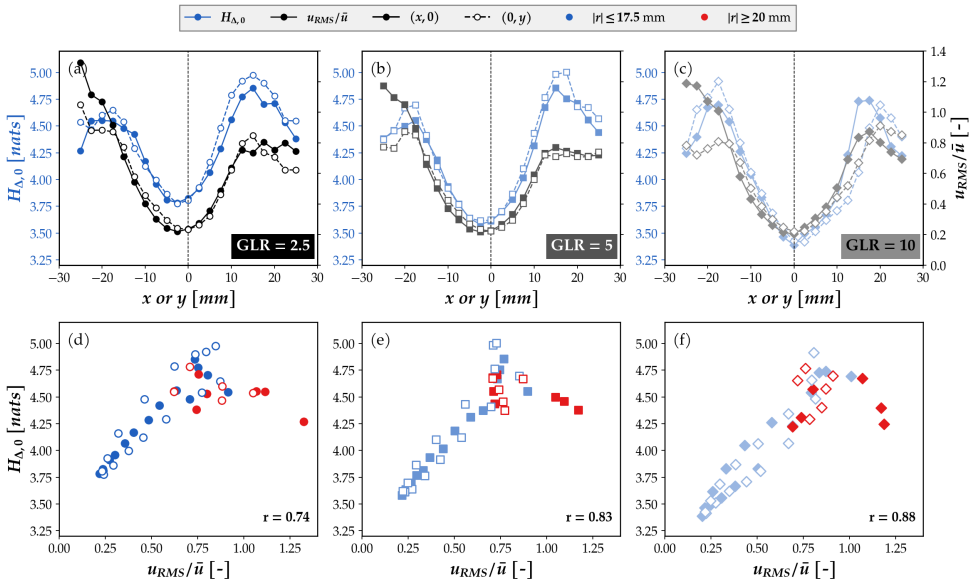


Fig. 14 Differential informature of the number-weighted distribution, $H_{\Delta,0}$ (blue, left axis), and relative fluctuation of the axial droplet velocity, $u_{RMS}/\bar{u}$ (black, right axis), along the $(x, 0)$ (filled symbols) and $(0, y)$ (open symbols) traverses for GLR = (a) 2.5, (b) 5 and (c) 10%, and (d–f) $H_{\Delta,0}$ against $u_{RMS}/\bar{u}$ at the same points, with the points at $|r| \geq 20$ mm in red; r is the correlation coefficient over all points of each condition.

In summary, computed from droplet sizes alone, the differential informature locates the edge of the entraining gas jet, where the mean droplet velocity reaches its peripheral plateau, and beyond it distinguishes the coexistence of small and large droplets from a few fast droplets crossing a slow gas, a distinction that neither the mean diameters nor $u_{RMS}/\bar{u}$ make.

5.3 Second infodynamic pattern: three regions of information carriers

The results concerning the Representation Index $R_{(j)}$ for the three GLR conditions, computed with Eq. (12), together with the combined indices are shown in Fig. 15. Despite the different GLR conditions, a second infodynamic pattern emerged that allows three regions to be distinguished. Through Eq. (12), each single index locates its carrier relative to $D_{\times}$, and, since $D_{g,0} \leq D_{g,2} \leq D_{g,3}$, the highest single index belongs to the carrier whose $D_{g,j}$ lies closest to $D_{\times}$. As the droplets become larger away from the axis, $D_{g,3}$, $D_{g,2}$ and $D_{g,0}$ reach $D_{\times}$ in this order, at about 7.5, 12.5 and 20 mm from the axis for GLR = 10%, which delimits the three regions. In the outer region, $|x| \gtrsim 20$ mm, the information is mostly carried by the number of droplets, with $R_{(0)}$ reaching 0.9–0.99. The small droplets are scarce there, since they follow the gas and remain within the jet: in median over the outer positions, 5% of the droplets

are smaller than 40 μm and 92% lie between 40 and 150 μm. These droplets, which reach the outer region on their own inertia, form a narrow population whose number-weighted geometric mean diameter, $D_{g,0} = 69$ μm in median, is close to $D_\times = 67$ μm, which makes $R_{(0)}$ high. The fraction of droplets with low Stokes numbers does increase towards this region by up to two orders of magnitude (see details in Sec. 5.4), but only up to 15–17.5 mm from the axis, at the edge of the gas jet, where they coexist with the large droplets. In the intermediate region, approximately 7.5–17.5 mm from the axis, the small droplets carried by the jet and the large droplets moving on their own inertia overlap, as discussed above for the differential informature. The number carrier then lies below $D_\times$ and the volume carrier above it, whereas the area carrier lies close to $D_\times$, resulting in elevated $R_{(2)}$ (0.90–0.97), while $R_{(0,2,3)}$ falls to 0.13–0.31 because the number and volume carriers reside at separated scales.

In the central region, the volume/mass carriers are the most represented, and this region widens as GLR increases. At GLR = 2.5%, $R_{(3)}$ peaks on the axis, and this condition also produced the largest fraction of droplets exceeding 250 µm. As GLR increases at constant injection pressure, the gas core accelerates, and the large droplets are progressively depleted from the axis. At GLR = 5%, $R_{(3)}$ remains high around the axis, whereas at GLR = 10% it drops to 0.42 on the axis and peaks off-axis, at $|x| \approx 5$–10 mm, and $R_{(0,2,3)}$ reaches 0.04. On the axis, however, the three carriers lie below $D_\times$ ($D_{g,0}$, $D_{g,2}$ and $D_{g,3}$ of 16, 24 and 29 μm), as in the narrow population of Sec. 3, so this low value reflects a population of small droplets far below the reference scale rather than a separation of scales. Read through Eq. (12), the decrease of $R_{(3)}$ on the axis is the decrease of $D_{g,3}$ there, from 87 μm at GLR = 2.5% to 46 and 29 μm at GLR = 5 and 10%, which crosses $D_\times$ between the first two conditions.

Since $R_{(3)}$ is largest where $D_{g,3} = D_\times$, the off-axis peak at GLR = 10% marks the radius, $|x| \approx 7.5$ mm, at which the volume carriers reach the reference scale, displaced outwards as the population on the axis becomes finer. The central $R_{(3)}$ dip, incipient at GLR = 5% and well defined at 10%, thus records a continuous change within one regime of annular discharge, not a change of regime.

Returning to the analogy of Sec. 3, if we read the spray like a screen, each radial position would be a pixel whose tone is set by whichever of the three informational subpixels dominates: number in the outer region, interfacial area in the intermediate region, and volume in the core, where the volume subpixel progressively dims on the axis as GLR increases. The bottom row of Fig. 15 takes this metaphor literally: each measurement point becomes a pixel whose red, green and blue intensities are $R_{(0)}$, $R_{(2)}$ and $R_{(3)}$, so that the three single profiles discussed separately above merge into one image of the informational structure of the spray, pale and reddish in the outer region, green in the intermediate region, and blue in the core, a blue that darkens on the axis as GLR increases.

The low $R_{(j)}$ values near the spray axis at high GLR values are not a sampling artefact. The axial positions have the largest samples, with 35 000 validated droplets, and, since Eq. (12) is evaluated droplet by droplet, $R_{(j)}$ involves no binning of the data and is therefore free from the sparse-class errors that affect the informature estimates of Eq. (10). The two measurement alphabets enter only through $D_\times$ because its definition, Eq. (11), already contains the rule by which each alphabet is built. Since

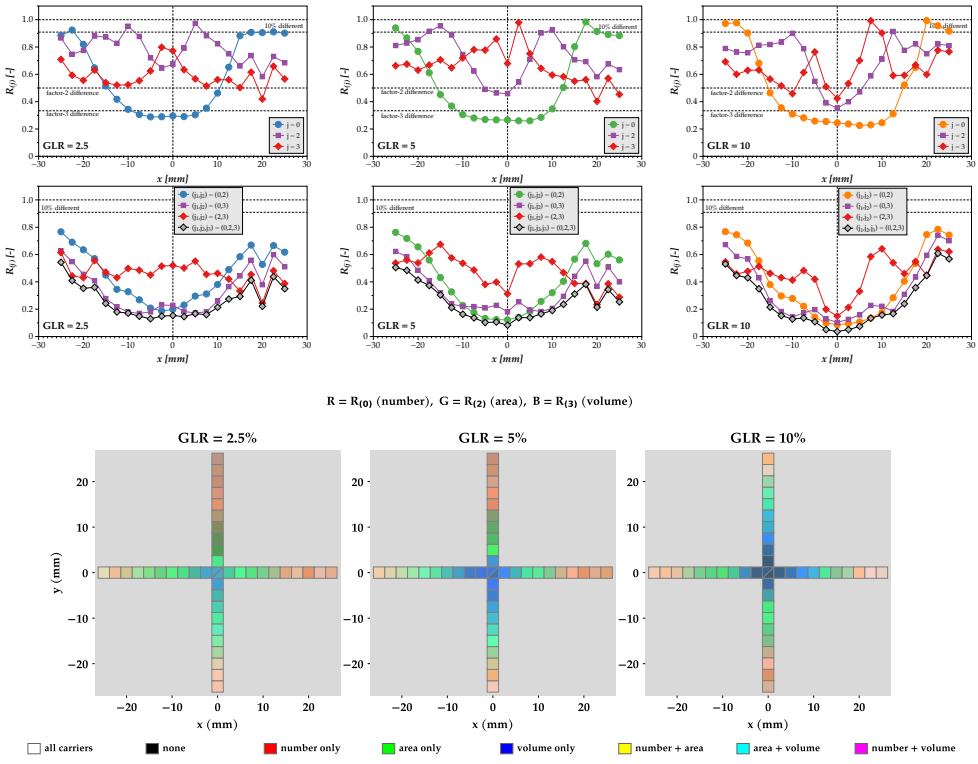


Fig. 15 Representation Index $R_{(j)}$, computed with Eq. (12), along the x-axis traverse for the three GLR conditions (top), combined indices (middle), and RGB map of the single indices along the $(x, 0)$ and $(0, y)$ traverses (bottom), in which the red, green and blue intensities of each square are $R_{(0)}$, $R_{(2)}$ and $R_{(3)}$. Each square is centred on a measurement point and extends half the distance to the adjacent points; the central square is split between the $(x, 0)$ (lower right) and $(0, y)$ (upper left) measurements.

both alphabets span the measurement domain of the PDI configuration, $D_\times$ is common to all positions, and a local decrease in $R_{(j)}$ reflects the distribution of information carriers at that position rather than a change in the reference against which it is measured. These low values may nevertheless be partially affected by measurement limitations. In the dense spray center, signal losses for small droplets may reduce the number of validated events and alter the apparent size distributions. Such losses would remove the finest droplets from the sample and increase the geometric mean diameters $D_{g,j}$. Where $R_{(j)}$ decreases in the center, these diameters lie below $D_\times$ (16, 24 and 29 μm on the axis at GLR = 10%), so that the losses would move them towards $D_\times$ and raise $R_{(j)}$. The measured central decrease of $R_{(j)}$ therefore underestimates the actual one: with all the small droplets detected, it would be at least as pronounced.

5.4 Stokes number interpretation of the infodynamic regions

To provide a spray dynamic interpretation of the observed infodynamic regions, a local Stokes number analysis was performed using raw PDI data. The particle relaxation time was computed as $\tau_p = \rho_l d^2/(18\mu_g)$, and the characteristic flow time scale as $\tau_f = b_{1/2}/U_G$, where U_G is the local gas velocity and $b_{1/2}$ the half-width of the round jet at the measurement plane, yielding the local Stokes number $\mathrm{St} = \tau_p/\tau_f$ for each droplet. At $z = 100$ mm, about $83\,d_o$, the large eddies that a droplet has to follow scale with $b_{1/2}$, not with the nozzle diameter, and in the far field of particle-laden jets and twin-fluid sprays the droplet response is described by a Stokes number based on the large-eddy time scale (Prévost et al. 1996; Huck et al. 2022) or on the centreline velocity and the half-width (Haghshenas et al. 2022). With $b_{1/2} = 0.094\,z = 9.4$ mm, from the laser-Doppler measurements of Hussein et al. (1994), τ_f is 0.36–0.54 ms on the axis, whereas the mean flow of a jet changes over $z/U_G \approx 10\,\tau_f$, 3.8–5.7 ms, which is also the flight time from the nozzle. The three Stokes ranges then acquire a definite meaning: tracer-like droplets ($\mathrm{St} < 0.1$) follow the large eddies, and therefore both the mean gas velocity and its fluctuations; transitional droplets ($0.1 \leq \mathrm{St} \leq 10$) lag the eddies but have $\tau_p < z/U_G$, so they have relaxed to the mean gas velocity since leaving the nozzle; and ballistic-like droplets ($\mathrm{St} > 10$) have $\tau_p > z/U_G$, longer than their flight time, so they retain the velocity of the discharge. On the axis, the ballistic-like threshold corresponds to $d \approx 35$ µm.

U_G was estimated at each point from the droplets that are both response-capable and part of a coherent velocity population, following the algorithm of Appendix B. It could be evaluated at 92 of the 126 measurement points, and 81 of them passed all the reliability tests of the appendix (20, 29 and 32 at GLR = 2.5, 5 and 10%), up to 17.5–25 mm from the axis. Fig. 16 verifies the classification with the measurements themselves. Droplets of 5–12 µm have the same median velocity at every point, a plateau that can only be the gas velocity, and U_G differs from it by 2.3% in median. The median velocity of the transitional droplets follows U_G within 6% across the whole profile, whereas the ballistic-like droplets move at 1.6–2.1 times U_G in median and keep 13–15 m/s at the spray edge, where the gas has slowed down to 1–3 m/s (Fig. 16a). Plotted against the Stokes number of each size class, the velocity departs from U_G at $\mathrm{St} \approx 4$ in median (interquartile range 3–6), inside the transitional range, which confirms that transitional droplets follow the mean flow and ballistic-like droplets do not (Fig. 16b). At the spray edge, where the gas is slow, the upper part of the transitional range includes droplets larger than about 70 μm that still move three to six times faster than the gas, consistent with the departure at $\mathrm{St} \approx 4$. Normalized by their values on the axis and by their half-widths, 7.7–8.4 mm, the U_G profiles of the three GLR conditions collapse onto a single Gaussian-like profile (Appendix B), as in round jets (Hussein et al. 1994), slightly narrower, as expected for droplet-laden jets (Hetsroni and Sokolov 1971).

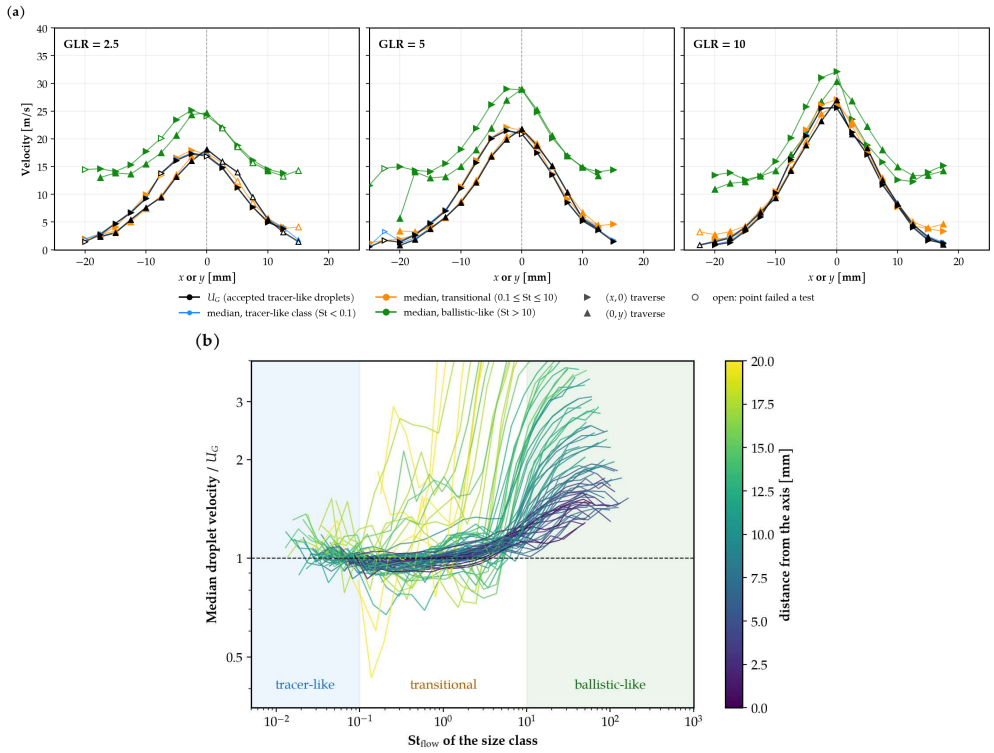


Fig. 16 (a) Profiles of U_G and of the median velocity of the tracer-like, transitional and ballistic-like droplets for GLR = 2.5, 5 and 10% along the $(x, 0)$ (▶) and $(0, y)$ (▲) traverses; open symbols: points that failed a reliability test (Appendix B). (b) Median velocity of each size class divided by U_G against the Stokes number of the class, at the 81 points that passed all the tests, coloured by distance from the axis.

The number fractions of the three classes count droplets, whereas $R_{(j)}$ concerns the information carriers of number, interfacial area and volume. The link between the two descriptions appears when each Stokes class is weighted as the j-weighted distributions are, that is, when the share of the number ($j = 0$), surface area ($j = 2$) and volume ($j = 3$) carried by each dynamic class is computed at each point (Fig. 17). Transitional droplets dominated the whole cross-section, with 77–98% of the droplets at every reliable point, so that most droplets responded only partially to the gas motion. The tracer-like fraction was lowest on the axis, about 0.2% for the three GLR conditions, and increased by up to two orders of magnitude towards the spray edge, reaching 6%, 11% and 20% at 15–17.5 mm from the axis for GLR = 2.5, 5 and 10%, at the outer edge of the intermediate region. This rise marks the edge of the gas jet, where the small droplets that follow the decelerating gas meet the large droplets that move on their own inertia. Beyond it, in the outer region, small droplets are scarce. The ballistic-like fraction decreased on the axis as GLR increased, from 8.7% at GLR =2.5% to 6.3% and 4.4% at GLR = 5 and 10%, and was largest at 10–12.5 mm from the axis (20%, 13% and 10%).

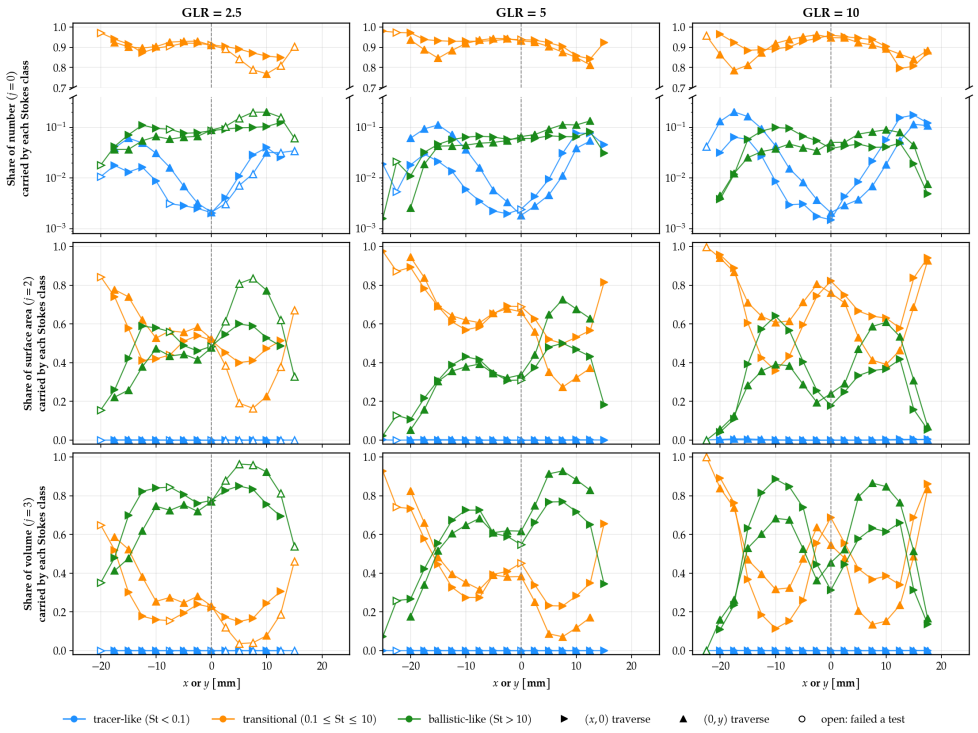


Fig. 17 Share of the number ($j = 0$, top, with the vertical axis broken into a linear part above and a logarithmic part below), surface area ($j = 2$, middle) and volume ($j = 3$, bottom) of the droplets carried by the tracer-like (St < 0.1), transitional and ballistic-like (St > 10) classes along the $(x, 0)$ (►) and $(0, y)$ (▲) traverses for GLR $= 2.5$, 5 and 10%, with St $= \tau_p U_G / b_{1/2}$. Open symbols: points that failed a reliability test (Appendix B).

Read side by side, Figs. 15 and 17 show which dynamic population holds each kind of information. The number is always held by the droplets that have relaxed to the gas, since the transitional droplets carry at least 77% of it at every point. Therefore, $R_{(0)}$, and every combined index that includes it, reads the population carried by the gas. Inside the gas jet, this population is fine and $R_{(0)}$ is low, while at the edge of the jet, where the fine droplets remain with the decelerating gas and mainly the droplets that arrive on their own inertia are left, $R_{(0)}$ rises, and $R_{(0,2)}$ and $R_{(0,3)}$ rise with it. The volume, instead, is held by the ballistic-like droplets wherever they are present, and $R_{(3)}$ and $R_{(2,3)}$ read this inertial population. At GLR $= 2.5\%$, the ballistic-like droplets carry most of the volume across the whole core, and $R_{(2,3)}$ is nearly flat there. At GLR $= 10\%$, the faster gas core depletes them from the axis, the volume passes largely to the transitional droplets, and $R_{(2,3)}$ drops on the axis and rises again off-axis, where the ballistic-like droplets again carry most of the volume. The interfacial area lies between the two because it is shared by the transitional and ballistic-like droplets, which is why $R_{(2)}$ is the highest single index in the intermediate region, where both populations coexist.

This reading also explains why $R_{(0,2,3)}$ is low both in the intermediate region and on the axis, especially at high GLR, for different reasons that the graphs themselves distinguish. In the intermediate region, the number is held by the droplets carried by the gas and the volume by the inertial ones, two populations with distinct dynamic responses, while area and volume still share the inertial population, so that $R_{(2,3)}$ remains high as $R_{(0,2)}$ and $R_{(0,3)}$ fall. On the axis at GLR = 10%, the three kinds of information are held mostly by droplets carried by the gas, all at sizes well below $D_\times$, and $R_{(2,3)}$ falls with the other indices. A low $R_{(0,2,3)}$ with a high $R_{(2,3)}$ thus marks the coexistence of gas-carried and inertial droplets, whereas a low $R_{(0,2,3)}$ with a low $R_{(2,3)}$ marks a fine population carried by the gas alone.

The two analyses describe the same spray from different data processing. The Stokes number classifies each droplet by its dynamic response, but requires the local gas velocity, which could be estimated at 92 of the 126 points, and its classes lose their dynamic meaning at the edge of the jet, where the gas is slow. The Representation Index is computed from the droplet sizes alone, at every point. Where both are available, they read the same structure, namely which dynamic population holds the number, the interfacial area and the volume of the spray. The Stokes analysis thus validates the infodynamic reading, and the infodynamic reading extends the Stoke analysis to where the dynamic classification is unfeasible.

6 Conclusions

This study investigated the infodynamic patterns emerging from the characterization of effervescent sprays, moving beyond the mean droplet diameters and conventional statistical descriptors to capture the informational structure associated with droplet size diversity. By using part of the Shannon measure of information (informature), its intensive counterpart in the differential informature, and introducing the Representation Index $R_{(j)}$, we developed a novel characterization layer capable of expressing aspects of spray indeterminacy that are hidden when the droplet size distribution is reduced to a single mean value.

The analysis showed that the measurement alphabet used to organize droplet sizes into classes affects the informature obtained from the number-, area-, and volume-weighted droplet size distributions. Regular and variable size classes can represent the same droplet sample with similar mean diameters but different amounts of information (informature) because they construct different (most probable) macrostates from the same spray microstates. In contrast, the differential informature, which includes the class-size contribution through the probability density, remained essentially independent of the measurement alphabet. This makes differential informature a more appropriate intensive parameter for describing the intrinsic informational structure of a measured spray.

The Representation Index $R_{(j)}$ was proposed to quantify the invariance of the Activation Factor with respect to the measurement alphabet. The Activation Factor represents the fraction of effective size classes that actively carry a given number-, area-, or volume-weighted view of the droplet size distribution. Separating the informature into its intensive and extensive parts yields a leading-order form of the index that can

be evaluated droplet by droplet, free from the discretization and sampling errors of the two informature estimates, while preserving its meaning. In this form, $R_{(j)}$ locates the j-weighted geometric mean diameter, $D_{g,j}$, relative to a reference scale set by the measurement domain, $D_{\times}$, so that a single index indicates where a carrier of a certain kind of information resides, not whether the spray is coherent. Scale separation is revealed by the differences between information carriers and by the combined indices.

The application of the framework to PDI measurements of an effervescent atomizer at different gas-to-liquid ratios (GLR) revealed a consistent radial infodynamic structure. Differential informature exposed an "info-hollow-cone" spray, with lower differential informature values near the center and higher values close to the spray/ambient interface. This structure indicates that the centerline region is characterized by a narrower morphological (droplet size) diversity, because the high-speed gas core carries the small droplets while the large ones move on their own inertia towards the periphery, whereas the spray boundary, where both populations coexist, contains a richer diversity of droplet sizes. The location of the differential-informature peak was consistent with the expected spray cone boundary, indicating that the spray/ambient interface could be identified from the informational structure of the droplet size distribution alone.

The radial profiles of $R_{(j)}$ revealed a second infodynamic pattern made of three regions. In the outer spray region, the density of droplets predominantly carried the spray information, because the droplets that reach this region on their own inertia form a narrow population centred close to the reference scale of the measurement. In the intermediate region, where the small droplets carried by the jet and the large droplets moving on their own inertia overlap, the area carrier lay close to the reference scale, with elevated $R_{(2)}$ values, while the number and volume carriers resided at separated scales. The local Stokes-number analysis showed the same separation in the dynamic response, with the number carried by transitional droplets and the volume by ballistic-like droplets there. In the central region, the volume/mass carriers were the most represented, but they were progressively depleted from the axis as GLR increased: $R_{(3)}$ peaked on the axis at GLR = 2.5%, whereas at GLR = 10% it dipped on the axis and peaked off-axis. Since the three conditions share the annular discharge regime, this depletion follows the decrease of the volume-weighted geometric mean diameter on the axis below $D_{\times}$ as the gas core accelerates with GLR. The local gas velocity, estimated from response-coherent tracer-like droplets with a Stokes number based on the jet half-width, followed a self-similar profile for the three GLR conditions, which supports this dynamic interpretation.

Overall, the proposed infodynamic approach provides a physically grounded methodology for characterizing the indeterminacy of complex two-phase spray systems. Differential informature describes the spatial organization of droplet size diversity, whereas the Representation Index identifies whether the number, interfacial area, and liquid volume are carried by coherent or scale-separated droplet populations. Introducing a novel characterization layer does not replace conventional spray quantities such as D_{10}, D_{32}, or D_{43}, but complement them by quantifying how the measured droplet size distribution conveys information across physically meaningful, weighted perspectives. Such information can support a more rigorous validation of numerical

models by comparing not only the mean sizes and velocities but also the informational content generated by atomization, transport, and gas–liquid interaction mechanisms.

Acknowledgements

The authors O.C., M.M., and J.J. acknowledge the financial support from project No. 25-17759S, funded by the Czech Science Foundation. M.O.P. acknowledges that this research was also funded in part by the Fundação para a Ciência e a Tecnologia, I.P. (FCT) under Grant UID/50022/2025 and LA/P/0079/2020. For the purpose of Open Access, the author has applied a CC-BY public copyright license to any Author Accepted Manuscript (AAM) version arising from this submission.

Nomenclature

$b_{1/2}$	Half-width of the round jet at the measurement plane [mm]
d_i	Droplet diameter in class i [μm]
d_k	Droplet diameter [μm]
d_o	Atomizer exit-orifice diameter [m]
D_0	Lower edge of the geometric progression of the variable classes, 1 μm [μm]
D_l	Diameter class edge indexed by l [μm]
D_{10}	Arithmetic mean diameter [μm]
D_{32}	Sauter Mean Diameter (SMD) [μm]
D_{43}	Volume-weighted mean diameter [μm]
D_{50}	Median diameter of a log-normal distribution [μm]
$D_{j,10}$	10th percentile diameter of the j-weighted DSDn [μm]
$D_{j,50}$	50th percentile diameter of the j-weighted DSDn [μm]
$D_{j,90}$	90th percentile diameter of the j-weighted DSDn [μm]
D_{max}	Upper limit of the PDI measurement domain [μm]
D_{min}	Lower limit of the PDI measurement domain [μm]
$D_{\alpha j}$	$(\alpha - j)$-moment diameter of a j-weighted DSDn [μm]
D_{mj}	Mean diameter associated with a j-weighted DSDn [μm]
$D_{g,j}$	Geometric mean diameter of the j-weighted DSDn [μm]
D_{JS}	Jensen–Shannon divergence between the size distributions of two droplet populations, Eq. (B6
$D_\times$	Crossover diameter between regular and variable classes [μm]
$F_{j,i}$	Cumulative distribution of the j-weighted DSDn [-]
G_j	Grid term of the differential informature of the j-weighted distribution, Eq. (6) [nats]
$H_{I,j}$	Informature of the j-weighted distribution [nats]
$H_{\Delta,j}$	Differential informature of the j-weighted distribution [nats]
j	Weight type index: 0 (number), 2 (area), 3 (volume) [-]
J	Interlaced Fibonacci series index [-]
k	Number of classes/bins [-]
$k_{eff,j}$	Number of effective classes for the j-weighted distribution, $\exp(H_{I,j})$ [-]
l	Class-edge index [-]
m	Mean-diameter order index [-]
$m_{j,\ell}$	Moment of order ℓ of the j-weighted distribution [μm$^\ell$]

n_i	Number of droplets in class i [-]
N	Total number of droplets [-]
p_{in}	Inlet pressure [Pa]
$p_{j,i}$	Probability density of class i in the j-weighted distribution [$\mu\mathrm{m}^{-1}$]
q	Weibull shape factor or fractal-dimension parameter [-]
R_e	Average ratio between adjacent class limits [-]
$R_{(j)}$	Representation Index for the j-weighted distribution [-]
$R_{(j_1,j_2,\ldots)}$	Combined Representation Index for multiple weighted distributions [-]
s	Standard deviation of $\ln D$ in a log-normal distribution [-]
SR	Size range, D_{max}/D_{min} [-]
St	Stokes number [-]
$\bar{u}$	Mean axial droplet velocity at a measurement point [m/s]
u_i	Droplet velocity [m/s]
u_{RMS}	Root-mean-square fluctuation of the axial droplet velocity [m/s]
U_G	Continuous phase velocity [m/s]
$U_{G,\mathrm{axis}}$	Continuous phase velocity on the spray axis [m/s]
w	Weight fraction [-]
x_i	Droplet-level state vector, $x_i \equiv (d_i, u_i)$ [-]
x, y, z	Measurement coordinates [mm]

Greek Letters

α	Moment-diameter order index [-]
Δd_i	Class size [μm]
$\Delta x, \Delta y$	Measurement spacing in the x- and y-directions [mm]
η_j	Linearized ratio of Activation Factors, $\eta_j = \ln(\rho_j)$ [-]
μ_g	Dynamic viscosity of the gas phase [Pa s]
ξ	Coordinate normalized by the half-width of the U_G profile [-]
ρ_j	Ratio of Activation Factors, $\rho_j = \phi_j^{(V)}/\phi_j^{(R)}$ [-]
σ_u	Standard deviation of the accepted droplet velocities [m/s]
ρ_g	Air density in the mixing chamber [$\mathrm{kg\,m^{-3}}$]
ρ_l	Liquid density [$\mathrm{kg\,m^{-3}}$]
τ_f	Characteristic flow time scale [s]
τ_p	Particle relaxation time [s]
ζ_k	Number fraction of droplet population k (1: inertial, 2: gas-carried) [-]
Ω	Spray microstate [-]
$\phi_j^{(MA)}$	Activation Factor for measurement alphabet MA [-]
φ	Golden ratio, $(1+\sqrt{5})/2$ [-]
$\omega_{j,i}$	Relative frequency of class i in the j-weighted distribution [-]

Acronyms

DSDn	Droplet Size Distribution
DSDy	Droplet Size Diversity
GLR	Gas-to-Liquid Ratio
GSD	Geometric Standard Deviation
MA	Measurement Alphabet

PDI	Phase Doppler Interferometry
PDF	Probability Density Function
RSF	Relative Span Factor
SCA	Spray Cone Angle
SDv	Volume-weighted Standard Deviation
SMD	Sauter Mean Diameter

Appendix A Derivation of Eq. (12)

Both measurement alphabets partition the same size range, $[D_{min}, D_{max}]$, into the same number of classes k given by Eq. (8). Using Eqs. (7)–(10), k cancels in the ratio of Activation Factors, and

$$\eta_j = \ln \frac{k^{(V)}_{eff,j}}{k^{(R)}_{eff,j}} = H^{(V)}_{I,j} - H^{(R)}_{I,j}. \tag{A1}$$

Writing each informature through Eq. (6) as $H_{I,j} = H_{\Delta,j} - G_j$,

$$\eta_j = \left(G^{(R)}_j - G^{(V)}_j\right) + \delta H_{\Delta,j}, \qquad \delta H_{\Delta,j} = H^{(V)}_{\Delta,j} - H^{(R)}_{\Delta,j}. \tag{A2}$$

The regular alphabet has a constant class width, $\Delta_R = (D_{max} - D_{min})/k$, hence $G^{(R)}_j = \ln \Delta_R$. The edges of the variable alphabet form a geometric progression, $D_l = D_{min}\, e^{lx}$ with $x = \ln R_e = \ln \varphi/(3J)$, so that the width of every class is proportional to its centre, $\Delta d_i = \beta d_i$ with $\beta = 2\tanh(x/2)$. Therefore,

$$G^{(V)}_j = \ln \beta + \sum_i \omega^{(V)}_{j,i} \ln d^{(V)}_i = \ln \beta + \ln D_{g,j}, \tag{A3}$$

that is, the grid term of the variable alphabet is the logarithm of the geometric mean diameter of the j-weighted DSDn, shifted by a constant. The ratio $\ln(SR)/x$ is, in general, not an integer, whereas k is, because Eq. (8) retains only its integer part. We therefore write $\ln(SR)/x = k + \theta$, where $0 \le \theta < 1$ is the decimal part discarded by the floor function, that is, the fraction of a class, on the logarithmic scale, that the k integer classes of ratio R_e leave uncovered in the size range. If R_e is adjusted to $SR^{1/k}$ once k is known, as in the processing code, the k classes span the size range exactly and $\theta = 0$. With this complement, k can be eliminated exactly, and $\Delta_R/\beta = D_\times(1 + \theta/k)\, x/[2\tanh(x/2)]$, with $D_\times$ given by Eq. (11). Substituting into Eq. (A2) gives

$$\eta_j = \ln \frac{D_\times}{D_{g,j}} + \ln\left(1 + \frac{\theta}{k}\right) + \ln \frac{x}{2\tanh(x/2)} + \delta H_{\Delta,j}. \tag{A4}$$

Eq. (A4) is exact, except for a boundary term proportional to the weight of the last variable class, which appears when that class is extended up to D_{max} to cover

the fraction θ and is negligible when little information resides at the upper end of the size range. All terms after the first are small corrections: $\ln(1+\theta/k) \le 1/k$; $\ln[x/(2\tanh(x/2))] \simeq x^2/12$ (2.4×10^{-4} for $J=3$), which follows from the Taylor expansion $x/[2\tanh(x/2)] = 1 + x^2/12 - x^4/720 + \cdots$ about $x=0$, together with $\ln(1+u)\simeq u$ for small u; and $\delta H_{\Delta,j} = O(1/k^2)$ for sufficiently large samples, because both alphabets estimate the same differential informature of the underlying continuous distribution, provided that the j-weighted DSDn spans several classes of both alphabets. For a population narrower than a few regular classes, the regular alphabet resolves it poorly, and $\delta H_{\Delta,j}$ is no longer small: for the narrow population at 20 μm of Fig. 5, $k^{(R)}_{eff,0} = 2.6$ and $\delta H_{\Delta,0} = -0.11$ with $J=3$, decreasing to -0.03 with $J=6$ ($k^{(R)}_{eff,0} = 4.7$) and -0.01 with $J=10$ ($k^{(R)}_{eff,0} = 7.7$). Eq. (12) does not contain this term, which is a further reason to evaluate $R_{(j)}$ with it. The number of classes, and therefore J, enters only through these corrections. Retaining the leading term in $R_{(j)} = \exp(-|\eta_j|)$ yields Eq. (12), which is equivalent to $R_{(j)} \simeq \min(D_\times, D_{g,j})/\max(D_\times, D_{g,j})$. As the classes are refined, $D_{g,j}$ tends to the j-weighted geometric mean of the droplet sample, $\exp\left(\sum_n D_n^j \ln D_n / \sum_n D_n^j\right)$, where D_n is the diameter of each droplet, which allows Eq. (12) to be evaluated droplet by droplet.

Appendix B Algorithm to obtain the continuous phase velocity U_G and coexistence of droplet populations

The continuous phase velocity U_G was estimated locally from the raw PDI samples using a response-coherent tracer-selection method without imposing a fixed droplet-size threshold. Droplets representative of the continuous phase must (1) be dynamically capable of responding to the gas flow within the flow time scale and (2) belong to a locally coherent velocity population. The first condition is the classical response-time Stokes number; the second avoids estimating U_G from isolated droplets or from droplets with distinct hydrodynamic histories.

For each valid PDI droplet event (d_k, u_i), the particle relaxation time was computed, assuming Stokes drag, as

$$\tau_{p,k} = \frac{\rho_l d_k^2}{18\mu_g}, \tag{B1}$$

where ρ_l is the liquid density and μ_g the dynamic viscosity of the gas. The flow time scale is $\tau_f = b_{1/2}/U_G$, with $b_{1/2}$ the half-width of the round jet at the measurement plane, so that

$$\mathrm{St}_{\mathrm{flow},k} = \frac{\tau_{p,k} U_G}{b_{1/2}}. \tag{B2}$$

The half-width grows linearly with the axial distance at a rate of 0.086–0.102 in round turbulent jets (Wygnanski and Fiedler 1969; Panchapakesan and Lumley 1993; Hussein et al. 1994); we adopted $b_{1/2} = 0.094\,z = 9.4$ mm at $z = 100$ mm, from Hussein et al.

(1994), neglecting the virtual origin. The measured U_G profiles have half-widths of 8.4, 8.1 and 7.7 mm for GLR = 2.5, 5 and 10%, slightly narrower, as expected for droplet-laden jets (Hetsroni and Sokolov 1971); using 8.1 mm instead of 9.4 mm changes U_G by 1.7% in median and the class fractions by less than 4 percentage points. The nozzle diameter, which characterizes the droplet response at the jet exit (Lau and Nathan 2016), is not the scale of the gas motion at $83\,d_\mathrm{o}$ from the nozzle, where the Stokes number of a given droplet has decreased with the axial distance (Jedelský et al. 2018): with $d_\mathrm{o} = 1.2$ mm as the flow length, the response condition below would limit the tracer-like droplets to 1–5 µm, at the lower end of the PDI range, and U_G would rest on 5 to 64 droplets out of up to 35 000 at only 58 of the 126 measurement points.

Because U_G is not known a priori, the method was implemented iteratively. At iteration m, droplets were first tested for response capability,

$$\mathrm{St}_{\mathrm{flow},k}^{(m)} = \frac{\tau_{p,k} U_G^{(m)}}{b_{1/2}} < \mathrm{St}_\mathrm{tr} = 0.1, \tag{B3}$$

which selects droplets with a sufficiently short response time but does not prove that they are adequate tracers of the local gas velocity. A velocity coherence condition was then applied to the response-capable subset, with median velocity $\widetilde{U}^{(m)}$ and robust velocity scale

$$\sigma_\mathrm{rob}^{(m)} = 1.4826\,\mathrm{median}\left(\left|u_i - \widetilde{U}^{(m)}\right|\right), \tag{B4}$$

retaining the droplets with

$$\left|u_i - \widetilde{U}^{(m)}\right| \le C_\mathrm{MAD}\,\sigma_\mathrm{rob}^{(m)}, \qquad C_\mathrm{MAD} = 2.5. \tag{B5}$$

Eqs. (B4) and (B5) form a Hampel identifier, a robust outlier detection procedure well established in engineering data analysis (Pearson 2002) and the standard approach for validating velocity data in experimental fluid mechanics (Westerweel and Scarano 2005). The threshold $C_\mathrm{MAD} = 3$ of Pearson (2002) removes gross errors only; the present condition must also exclude valid droplets belonging to a different hydrodynamic population, so a slightly stricter value was adopted, which still retains 98.8% of a Gaussian population, against 99.7% for $C_\mathrm{MAD} = 3$. The estimate was then updated as the median velocity of the droplets satisfying both conditions, $U_G^{(m+1)} = \mathrm{median}(u_i)$, and the iteration was stopped when the accepted set became unchanged or U_G varied by less than a prescribed tolerance. At seven points, the accepted set alternated between two sets differing by the one or two droplets crossing the response threshold, whose diameter scales with $U_G^{-1/2}$ in Eq. (B3). Such a period-two cycle was taken as convergence, and U_G was computed from the union of the two sets. If fewer than five droplets satisfied the final combined criterion, U_G was not evaluated at that point.

The reliability of each estimate was assessed with a leave-one-out test, in which U_G was recomputed after removing each accepted droplet, the range of the resulting values defining an uncertainty interval, and with four consistency checks on the accepted droplets: (1) a standard deviation of their velocities not exceeding $0.30\,U_{G,\mathrm{axis}}$, where $U_{G,\mathrm{axis}}$ is the value of U_G on the spray axis; (2) a difference between their mean and

median velocities not exceeding $0.15\,U_{G,\mathrm{axis}}$; (3) an absolute correlation coefficient between their diameters and velocities not exceeding 0.30; (4) tracer, transitional and ballistic fractions changing by no more than 5 percentage points within the leave-one-out interval of U_G. These limits follow from the requirements of a tracer-like population.

A tracer-like droplet inherits the velocity fluctuations of the gas, which in round jets are about 0.3 of the centreline velocity on the axis and decrease towards the edge when referred to the centreline velocity (Wygnanski and Fiedler 1969; Panchapakesan and Lumley 1993; Hussein et al. 1994), whereas relative to the local mean velocity they increase without bound as the flow becomes intermittent (Nguyen and Oberlack 2024). Therefore, the spread was referred to $U_{G,\mathrm{axis}}$, common to all points of a profile, and a larger spread indicates a mixture of populations. The difference between the mean and the median of any distribution does not exceed one standard deviation (Hotelling and Solomons 1932), so the limit (2), half of this bound, rejects strongly skewed populations that the median absolute deviation does not remove. A correlation coefficient of 0.30 means that droplet size explains at most 9% of the velocity variance, so any residual inertial dependence is weak. The limit (4) ensures that the uncertainty in U_G does not alter the Stokes-number classification beyond a margin small compared with the differences discussed in Sec. 5. Points with at least ten accepted droplets were classified as reliable when the leave-one-out range of U_G did not exceed 10% of its value, and points with five to nine accepted droplets as tentative when this range did not exceed 15%.

U_G was evaluated at 92 of the 126 measurement points, and 81 passed all the tests with at least ten accepted droplets, and the median number of accepted droplets per point was 175, 268 and 296 for GLR = 2.5, 5 and 10%. Of the remaining eleven points, eight failed the correlation test, two did not converge and one exceeded the leave-one-out limit, which is why they are shown with open symbols in Sec. 5. Normalized by $U_{G,\mathrm{axis}}$ (17.5, 21.3 and 26.3 m/s for GLR = 2.5, 5 and 10%) and by their half-widths, the U_G profiles of the three GLR conditions collapse onto a single profile close to the Gaussian profile of round jets, and the spread of the accepted velocities, 0.16–$0.24\,U_{G,\mathrm{axis}}$ within one half-width of the axis and decreasing towards the edge, follows the shape of the axial turbulence intensity profile of round jets (Fig. B1). Neither result was imposed by the method, which estimates U_G independently at each point.

The sensitivity to the thresholds was assessed by halving each one and increasing it by 50%, one at a time and all together. The thresholds do not enter the estimation of U_G, so they changed neither U_G nor the class fractions at any point. The mean–median, class-fraction and leave-one-out limits, and the spread limit increased by 50%, changed no label. The correlation limit changed the label of 1 to 7 points per GLR, and halving the spread limit rejected 13 to 16 points per GLR, all within 10 mm of the axis, where the measured spread is 0.16–$0.24\,U_{G,\mathrm{axis}}$, that is, a limit stricter than the turbulence of the jet itself. C_{MAD} enters the estimation: with $C_{\mathrm{MAD}} = 2.0$ or 3.0, the median change in U_G was below 2%, with a maximum of 15% at a single point, the class fractions changed by less than 2 percentage points, and the labels of at most five points changed.

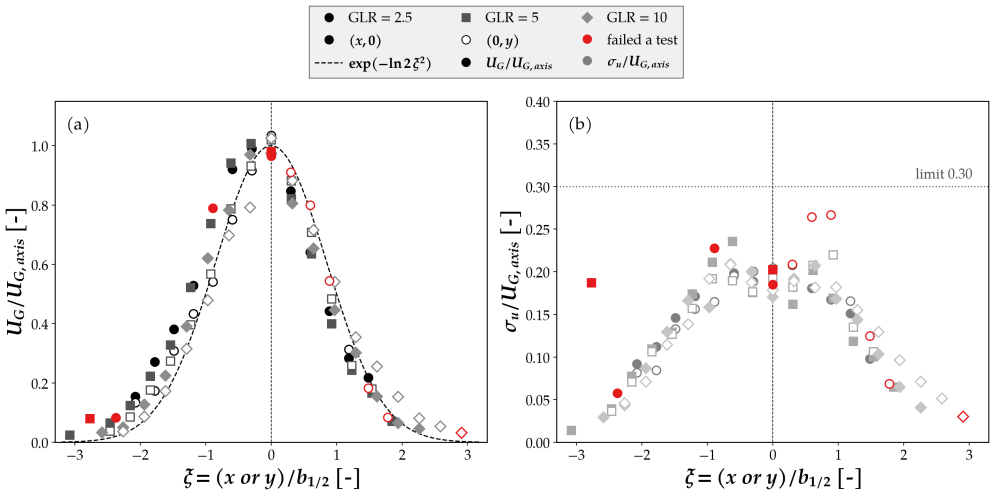


Fig. B1 (a) Continuous phase velocity U_G normalized by its value on the spray axis, and (b) standard deviation of the accepted droplet velocities normalized by $U_{G,\mathrm{axis}}$, against ξ, the coordinate along the $(x, 0)$ and $(0, y)$ traverses normalized by the half-width of each U_G profile. Circles, squares and diamonds: GLR = 2.5, 5 and 10%; filled symbols: $(x, 0)$; open symbols: $(0, y)$; red symbols: points that failed one of the tests. Dashed line in (a): Gaussian profile $\exp(-\ln 2\,\xi^2)$; dotted line in (b): limit of the velocity-spread test.

After obtaining U_G, all valid droplets at the same measurement point were classified with Eq. (B2) as tracer-like for $\mathrm{St}_{\mathrm{flow},k} < 0.1$, transitional for $0.1 \leq \mathrm{St}_{\mathrm{flow},k} \leq 10$ and ballistic-like for $\mathrm{St}_{\mathrm{flow},k} > 10$, and the counts were normalized by the total number of valid droplets at that point. This approach differs from the procedure of Rácz et al. (2022), who determined a critical droplet diameter from a relative-velocity Stokes number and recalculated the gas velocity from the droplets below it. Their method is a practical procedure when no independent gas-phase measurement is available, but it converts the tracer selection into a local diameter cut-off. In the effervescent spray used in this work, droplets of the same size may have different hydrodynamic histories, so the present method accepts droplets only when they are both response-capable and part of a coherent local velocity population.

Once U_G is known, the droplets at each point can also be split by velocity into two populations: those moving faster than $f\,U_G$, with $f = 2$, which reach the point on their own inertia, and the remaining ones, which move with the gas. Let ζ_1 and $\zeta_2 = 1 - \zeta_1$ be their number fractions and $\omega_{1,i}$ and $\omega_{2,i}$ their number-weighted size distributions over the same variable classes, so that the distribution of all droplets is $\omega_i = \zeta_1\omega_{1,i} + \zeta_2\omega_{2,i}$. Because both populations share the class widths, their grid terms combine linearly, and the differential informature of all droplets separates exactly as Eq. (14), with

$$D_{JS} = \sum_{k=1}^{2} \zeta_k \sum_i \omega_{k,i} \ln \frac{\omega_{k,i}}{\omega_i}, \tag{B6}$$

where D_{JS} is the generalized Jensen–Shannon divergence between the two size distributions (Lin 1991). D_{JS} measures the diversity added by the coexistence of fast and slow droplet populations. It is zero when the two populations have the same size distribution and reaches its maximum, $-\zeta_1 \ln \zeta_1 - \zeta_2 \ln \zeta_2$, when they occupy disjoint ranges of sizes, since then $\omega_i = \zeta_k \omega_{k,i}$ in every class occupied by population k, and the logarithm in Eq. (B6) reduces to $-\ln \zeta_k$. D_{JS} was computed at every point where U_G could be estimated, with $f = 1.5$, 2 and 3 to perform a sensivity analysis to the threshold chosen. For all three thresholds, D_{JS} is negligible within 7.5 mm of the axis and grows up to the radius of the $H_{\Delta,0}$ peak in all twelve half-profiles, which shows that this result does not depend on the threshold chosen to separate the two populations.

References

Beard, K.V.: Terminal velocity and shape of cloud and precipitation drops aloft. Journal of Atmospheric Sciences **33**(5), 851–864 (1976)

Chang, Y.-C., Calabrese, R.V., Gentry, J.W.: An algorithm for determination of the size-dependent breakage frequency of droplets, flocs and aggregates. Particle & Particle Systems Characterization **8**(1-4), 315–322 (1991)

Cejpek, O., Malý, M., Belka, M., Rácz, E., Hajek, J., Hajek, O., Jedelsky, J.: Spray–gas counterflow interactions in an absorber column. Separation and Purification Technology, 135926 (2026)

Cejpek, O., Malý, M., Dhinasekaran, V.K., Avulapati, M.M., Dacanay, L., Jedelský, J.: Novel atomizer concept for CCS applications: impinging effervescent atomizer. Separation and Purification Technology **311**, 123259 (2023)

Cejpek, O., Malý, M., Jedelský, J.: Combined drop sizing using phase doppler anemometry and high-speed imaging. In: AIP Conference Proceedings, vol. 2672, p. 020001 (2023). AIP Publishing LLC

Der Kiureghian, A., Ditlevsen, O.: Aleatory or epistemic? Does it matter? Structural Safety **31**(2), 105–112 (2009) https://doi.org/10.1016/j.strusafe.2008.06.020

Dumouchel, C.: The maximum entropy formalism and the prediction of liquid spray drop-size distribution. Entropy **11**(4), 713–747 (2009) https://doi.org/10.3390/e11040713

Ferrão, I.A., Panão, M.R., Mendes, M.A., Moita, A.S., Silva, A.R.: How different are conventional and biofuel sprays applied to aviation? an infodynamic comparative analysis. Experiments in Fluids **66**(6), 114 (2025)

García, J., Lozano, A., Alconchel, J., Calvo, E., Barreras, F., Santolaya, J.: Atomization of glycerin with a twin-fluid swirl nozzle. International Journal of Multiphase Flow **92**, 150–160 (2017)

Guildenbecher, D.R., López-Rivera, C., Sojka, P.E.: Secondary atomization. Experiments in Fluids **46**(3), 371–402 (2009) https://doi.org/10.1007/s00348-008-0593-2

Hussein, H.J., Capp, S.P., George, W.K.: Velocity measurements in a high-Reynolds-number, momentum-conserving, axisymmetric, turbulent jet. Journal of Fluid Mechanics **258**, 31–75 (1994) https://doi.org/10.1017/S002211209400323X

Heinlein, J., Fritsching, U.: Droplet clustering in sprays. Experiments in fluids **40**(3), 464–472 (2006)

Haghshenas, A., Hassanpour, M., Tabe, R., Eshghinejadfard, A.: Characterization of particle-laden jet flows in inertia-dominated regime. International Journal of Multiphase Flow **156**, 104245 (2022) https://doi.org/10.1016/j.ijmultiphaseflow.2022.104245

Huck, P.D., Osuna-Orozco, R., Machicoane, N., Aliseda, A.: Spray dispersion regimes following atomization in a turbulent co-axial gas jet. Journal of Fluid Mechanics **932**, 36 (2022) https://doi.org/10.1017/jfm.2021.992

Hotelling, H., Solomons, L.M.: The limits of a measure of skewness. The Annals of Mathematical Statistics **3**(2), 141–142 (1932) https://doi.org/10.1214/aoms/1177732911

Hetsroni, G., Sokolov, M.: Distribution of mass, velocity, and intensity of turbulence in a two-phase turbulent jet. Journal of Applied Mechanics **38**(2), 315–327 (1971) https://doi.org/10.1115/1.3408779

Hammad, F.A., Sun, K., Che, Z., Jedelský, J., Wang, T.: Internal two-phase flow and spray characteristics of outside-in-liquid twin-fluid atomizers. Applied Thermal Engineering **187**, 116555 (2021)

Jedelský, J., Jicha, M.: Energy conversion during effervescent atomization. Fuel **111**, 836–844 (2013)

Jedelský, J., Jicha, M., Slama, J., Otahal, J.: Development of an effervescent atomizer for industrial burners. Energy & Fuels **23**(12), 6121–6130 (2009)

Jedelský, J., Malý, M., Pinto del Corral, N., Wigley, G., Janáčková, L., Jícha, M.: Air–liquid interactions in a pressure-swirl spray. International Journal of Heat and Mass Transfer **121**, 788–804 (2018) https://doi.org/10.1016/j.ijheatmasstransfer.2018.01.003

Jedelský, J., Zaremba, M., Malý, M., Jícha, M.: Characteristics of droplet motion in effervescent sprays. In: EPJ Web of Conferences, vol. 67, p. 02050 (2014). EDP Sciences

Lefebvre, A.H.: A novel method of atomization with potential gas turbine applications. Defence Science Journal **38**(4), 353–362 (1988) https://doi.org/10.14429/dsj.38.5869

Lin, J.: Divergence measures based on the Shannon entropy. IEEE Transactions on Information Theory **37**(1), 145–151 (1991) https://doi.org/10.1109/18.61115

Lau, T.C.W., Nathan, G.J.: The effect of Stokes number on particle velocity and concentration distributions in a well-characterised, turbulent, co-flowing two-phase jet. Journal of Fluid Mechanics **809**, 72–110 (2016) https://doi.org/10.1017/jfm.2016.666

Li, X., Tankin, R.S.: On the prediction of droplet size and velocity distributions in sprays through maximum entropy principle. Particle & Particle Systems Characterization **9**(1) (1992) https://doi.org/10.1002/ppsc.19920090126

Malý, M., Cejpek, O., Hájek, J., Jedelský, J.: Pod analysis of stable and unstable effervescent spray. In: Proceedings Topical Problems of Fluid Mechanics, pp. 167–172 (2025). https://doi.org/10.14311/TPFM.2025.022

Mlkvik, M., Jedelský, J., Karbstein, H.P., Gaukel, V.: Spraying of viscous liquids: influence of fluid-mixing mechanism on the performance of internal-mixing twin-fluid atomizers. Applied Sciences **10**(15), 5249 (2020)

Nguyen, C.T., Oberlack, M.: Analysis of a turbulent round jet based on direct numerical simulation data at large box and high Reynolds number. Physical Review Fluids **9**(7), 074608 (2024) https://doi.org/10.1103/PhysRevFluids.9.074608

Panão, M.R.O.: Ultrasonic atomization: New spray characterization approaches. Fluids **7**(1), 29 (2022) https://doi.org/10.3390/fluids7010029

Panão, M.R.: On the infodynamics of ramifications in constructal design. Biosystems **248**, 105388 (2025)

Panão, M.: Exploring infodynamics in the study of human aerosol droplet size distributions. Physics of Fluids **37**(11) (2025)

Prévost, F., Borée, J., Nuglisch, H.J., Charnay, G.: Measurements of fluid/particle correlated motion in the far field of an axisymmetric jet. International Journal of Multiphase Flow **22**(4), 685–701 (1996) https://doi.org/10.1016/0301-9322(96)00009-2

Pearson, R.K.: Outliers in process modeling and identification. IEEE Transactions on Control Systems Technology **10**(1), 55–63 (2002) https://doi.org/10.1109/87.974338

Panchapakesan, N.R., Lumley, J.L.: Turbulence measurements in axisymmetric jets

of air and helium. Part 1. Air jet. Journal of Fluid Mechanics **246**, 197–223 (1993) https://doi.org/10.1017/S0022112093000096

Park, J., Lee, T.-W., Malý, M., Cejpek, O., Jedelský, J.: Determination of the drop size and distributions in swirl injection in cross flows, impinging, and effervescent injectors. Atomization and Sprays **34**(5) (2024)

Panão, M.O., Moita, A.S., Moreira, A.L.: On the statistical characterization of sprays. Applied Sciences **10**(17), 6122 (2020)

Roesler, T., Lefebvre, A.: Studies on aerated-liquid atomization. International Journal of Turbo and Jet Engines **6**(3-4), 221–230 (1989)

Rosell-Llompart, J., Gañán-Calvo, A.M.: Turbulence in pneumatic flow focusing and flow blurring regimes. Physical Review E—Statistical, Nonlinear, and Soft Matter Physics **77**(3), 036321 (2008)

Rácz, E., Malý, M., Jedelský, J., Józsa, V.: Gas-phase velocity estimation in practical sprays by phase-doppler technique. International Journal of Multiphase Flow **157**, 104260 (2022) https://doi.org/10.1016/j.ijmultiphaseflow.2022.104260

Shannon, C.E.: A mathematical theory of communication. The Bell system technical journal **27**(3), 379–423 (1948)

Sijs, R., Kooij, S., Holterman, H., Van De Zande, J., Bonn, D.: Drop size measurement techniques for sprays: Comparison of image analysis, phase doppler particle analysis, and laser diffraction. AIP advances **11**(1) (2021)

Schröder, J., Kraus, S., Rocha, B.B., Gaukel, V., Schuchmann, H.P.: Characterization of gelatinized corn starch suspensions and resulting drop size distributions after effervescent atomization. Journal of food engineering **105**(4), 656–662 (2011)

Sun, C., Ning, Z., Qiao, X., Lv, M., Li, Y., Zhao, J., Wang, X.: Study on effervescent spray morphology based on internal gas-liquid two-phase flow patterns. European Journal of Mechanics-B/Fluids **74**, 123–138 (2019)

Sovani, S.D., Sojka, P.E., Lefebvre, A.H.: Effervescent atomization. Progress in Energy and Combustion Science **27**(4), 483–521 (2001) https://doi.org/10.1016/S0360-1285(00)00029-0

Taitel, Y., Barnea, D., Dukler, A.E.: Modelling flow pattern transitions for steady upward gas-liquid flow in vertical tubes. AIChE Journal **26**(3), 345–354 (1980) https://doi.org/10.1002/aic.690260304

Villermaux, E., Marmottant, P., Duplat, J.: Ligament-mediated spray formation. Physical Review Letters **92**(7), 074501 (2004) https://doi.org/10.1103/PhysRevLett.92.074501

Wittner, M.O., Ballesteros, M.A., Link, F.J., Karbstein, H.P., Gaukel, V.: Air-core–liquid-ring (aclr) atomization part ii: Influence of process parameters on the stability of internal liquid film thickness and resulting spray droplet sizes. Processes **7**(9), 616 (2019)

Wygnanski, I., Fiedler, H.: Some measurements in the self-preserving jet. Journal of Fluid Mechanics **38**(3), 577–612 (1969) https://doi.org/10.1017/S0022112069000358

Westerweel, J., Scarano, F.: Universal outlier detection for PIV data. Experiments in Fluids **39**(6), 1096–1100 (2005) https://doi.org/10.1007/s00348-005-0016-6

Zhang, N., Calabrese, R.V., Gentry, J.W.: Fundamental properties of interlaced fibonacci sequences and their potential in describing particle breakage. Journal of Aerosol Science **23**, 193–196 (1992)

Zaremba, M., Kozák, J., Malý, M., Weiß, L., Rudolf, P., Jedelský, J., Jícha, M.: An experimental analysis of the spraying processes in improved design of effervescent atomizer. International Journal of Multiphase Flow **103**, 1–15 (2018)